

Isovolumetric Energy Minimization for Ball-Shaped Volume-Preserving Parameterizations of 3-Manifolds

Shu-Yung Liu¹, Tsung-Ming Huang¹, Wen-Wei Lin^{2,3,4}, and Mei-Heng Yueh¹

¹*Department of Mathematics, National Taiwan Normal University, Taipei, Taiwan*

²*Nanjing Center for Applied Mathematics, Nanjing, China*

³*Shanghai Institute for Mathematics and Interdisciplinary Sciences, Shanghai, China*

⁴*Department of Applied Mathematics, National Yang Ming Chiao Tung University, Hsinchu, Taiwan*

Abstract

A volume-preserving parameterization is a bijective mapping that maps a 3-manifold onto a specified canonical domain that preserves the local volume. This paper formulates the computation of ball-shaped volume-preserving parameterizations as an isovolumetric energy minimization (IEM) problem with the boundary points constrained on a unit sphere. In addition, we develop a new preconditioned nonlinear conjugate gradient algorithm for solving the IEM problem with guaranteed theoretical convergence and significantly improved accuracy and computational efficiency compared to other state-of-the-art algorithms. Applications to solid shape registration and deformation are presented to highlight the usefulness of the proposed algorithm.

Keywords. Simplicial surface, Simplicial mapping, Volume-preserving parameterization, Numerical optimization

AMS subject classifications. 65D18, 68U05, 68U01, 65D17

1 Introduction

The ball-shaped volume-preserving parameterization of a simply connected 3-manifold is a bijective mapping that maps the manifold to a solid unit ball while preserving local volumes. This mapping induces a global coordinate chart for the manifold, simplifying various processing tasks to those applicable to the solid unit ball. Such parameterizations are particularly useful in computational tasks involving complex geometric structures. The technique has been utilized to compute optimal mass transport (OMT) mappings [27], which are subsequently applied to process 3D medical images for brain tumor segmentation [19, 20]. Specifically, unit cube-shaped volume-preserving parameterizations of the brain images are employed in machine-learning applications. The preservation of local volume is crucial for accurately training models to infer the tumor region and measure tumor size.

Recent advanced algorithms for computing 3-manifold mappings include close-to-conformal deformations [5], the simplicial foliation method [4], polycube mappings [13], OMT-based methods [16, 24], scalable locally injective mappings [23], the simplex lifting method [6], foldover-free mappings [14], symmetric volume mappings [1], and the volumetric stretch energy minimization (VSEM) [28, 29, 17]. Among these algorithms, the OMT-based methods and the VSEM aim to compute ball-shaped volume-preserving parameterizations, similar to this paper. Specifically, the VSEM, which approaches the target mapping through numerical optimization, is the most relevant to our work. In the following, we introduce the pros and cons of the VSEM algorithm.

The volumetric stretch energy was first defined in [28] by heuristically imposing the volume-preserving condition to the volumetric discrete Dirichlet energy. This functional provides a global measurement of volume distortion for mappings, assuming the total volume of the domain and the image are the same. The volumetric stretch energy is equivalent to the sum of the scaled local volumes of tetrahedra with scaling factors being the Jacobian determinant

evaluated at those tetrahedra [17]. The theoretical minimal value of the energy is the total image volume, which occurs only at mappings with all local Jacobian determinants being one, i.e., volume-preserving mappings [17]. This concept is a generalization of the stretch energy [30, 26] for surface mappings and can also be extended to higher dimensional manifold mappings.

The previous VSEM algorithm [28, Algorithm 4.4] employed a fixed-point method that iteratively approaches critical points of the functional provided a Dirichlet boundary condition. This method can also be applied to 3-manifolds with boundaries being genus-one surfaces [29]. The boundary mapping in the VSEM algorithm is selected to be a spherical area-preserving mapping achieved by minimizing the stretch energy [30]. The stretch energy for surface mappings is the 2-dimensional analog of the volumetric stretch energy with the theoretical minimal value being the image area. The lower bound of the energy is attained only at area-preserving mappings [26].

The VSEM method is recognized as one of the most effective algorithms for maintaining the volume-preserving property. Still, the VSEM method has room to be improved. The convergence of the VSEM algorithm is not theoretically guaranteed. Also, the choice of fixed spherical area-preserving boundary mappings may not be optimal for ball-shaped volume-preserving mappings. In addition, the original VSEM method [17] assumes the total image volume is constant throughout the iteration process, which may not hold if the boundary points are allowed to glide along the unit sphere. To remedy these drawbacks, in this paper, we express the boundary mapping in spherical coordinates and optimize the whole mapping to find the best ball-shaped parameterization that reaches the least possible value of the objective functional. To compute a minimizer of the objective functional, we apply the nonlinear conjugate gradient (CG) method with suitable preconditioners. An appropriate generalization of the existing theoretical framework of numerical optimization can then guarantee the global convergence of this approach.

1.1 Contribution

This paper improves the problem formulation of the VSEM for computing ball-shaped volume-preserving parameterizations of simply connected 3-manifolds with robust theoretical support and proposes an efficient algorithm with guaranteed convergence. The main contributions of this paper are listed as follows:

- (i) We formulate the ball-shaped volume-preserving parameterizations as an isovolumetric energy minimization (IEM) problem with a spherical boundary shape constraint. The main difference between the IEM and the previous VSEM [28] is that the boundary mapping is not prescribed. In other words, the spherical boundary mapping is optimized simultaneously with the interior mapping to reach a parameterization with optimal volume distortions.
- (ii) We deal with the spherical boundary shape constraint by using the spherical coordinates, derive the associated explicit gradient formula, and develop a preconditioned nonlinear CG method for solving the IEM problem.
- (iii) A rigorous proof of the global convergence of the iterations in the proposed algorithm is provided. This proof can be regarded as a generalization of the convergence results for the nonlinear CG method introduced in [22, Chapter 5].
- (iv) Numerical experiments indicate that the effectiveness of decreasing the volume distortions is significantly improved compared to the previous VSEM algorithm [28], one of the most effective methods for computing ball-shaped volume-preserving parameterizations.
- (v) Applications of ball-shaped volume-preserving parameterizations to shape registration, deformation, and dissimilarity measurement of human brains are demonstrated to show the practical utility of the proposed algorithm.

1.2 Notation

In this paper, we use the following notation.

- \mathbb{R} denotes the set of real numbers.

- e denotes the identity mapping.
- Bold letters, e.g., \mathbf{f} , \mathbf{g} , \mathbf{p} , denote real-valued vectors or matrices.
- Capital letters, e.g., L , M , denote real-valued matrices.
- I_n denotes the identity matrix of size $n \times n$.
- Typewriter letters, e.g., \mathbf{I} , \mathbf{B} , denote ordered sets of indices.
- $n_{\mathbf{I}}$ denotes the number of elements of the set \mathbf{I} .
- \mathbf{f}_i denotes the i th entry or row of the vector or matrix \mathbf{f} .
- $\mathbf{f}_{\mathbf{I}}$ denotes the subvector or submatrix of \mathbf{f} composed of \mathbf{f}_i for $i \in \mathbf{I}$.
- $L_{i,j}$ denotes the (i,j) th entry of the matrix L .
- $L_{\mathbf{I},\mathbf{J}}$ denotes the submatrix of L , composed of entries $L_{i,j}$ for $i \in \mathbf{I}$ and $j \in \mathbf{J}$.
- The vector of length n with all entries being 0 and 1 is denoted by $\mathbf{0}_n$ and $\mathbf{1}_n$, respectively.

1.3 Organization of the paper

The remaining part of this paper is organized as follows. In Section 2, we introduce the simplicial 3-manifolds, mappings, and the isovolumetric energy functional. Then, we formulate the IEM problem for ball-shaped mappings and present the explicit formula of the energy gradient in Section 3. The preconditioned nonlinear CG method of the IEM is proposed in Section 4. The associated convergence analysis is provided in Section 5. Numerical experiments and comparisons to the state-of-the-art are presented in Section 6. Applications to volume-preserving registration and deformation are demonstrated in Section 7. Ultimately, concluding remarks are given in Section 8.

2 Simplicial 3-manifolds, mappings, and functionals

We introduce simplicial 3-manifolds, mappings, and the isovolumetric energy functional in subsections 2.1, 2.2 and 2.3, respectively.

2.1 Simplicial 3-manifolds

A simplicial 3-manifold \mathcal{M} is the underlying set of a homogeneous simplicial 3-complex, i.e., tetrahedral mesh, consisting of n vertices

$$\mathbb{V}(\mathcal{M}) = \{v_s = (v_s^1, v_s^2, v_s^3)^\top \in \mathbb{R}^3\}_{s=1}^n,$$

m tetrahedra

$$\mathbb{T}(\mathcal{M}) = \{\tau_t = [v_{i_t}, v_{i_t}, v_{k_t}, v_{\ell_t}] \subset \mathbb{R}^3 \mid v_{i_t}, v_{i_t}, v_{k_t}, v_{\ell_t} \in \mathbb{V}(\mathcal{M})\}_{t=1}^m,$$

triangular faces

$$\mathbb{F}(\mathcal{M}) = \{[v_i, v_j, v_k] \mid [v_i, v_j, v_k, v_\ell] \in \mathbb{T}(\mathcal{M}) \text{ for some } v_\ell \in \mathbb{V}(\mathcal{M})\},$$

and edges

$$\mathbb{E}(\mathcal{M}) = \{[v_i, v_j] \mid [v_i, v_j, v_k] \in \mathbb{F}(\mathcal{M}) \text{ for some } v_k \in \mathbb{V}(\mathcal{M})\},$$

where $[v_0, \dots, v_k]$ denotes the k -simplex with vertices v_0, \dots, v_k . Simplicial 3-manifolds are known as tetrahedral meshes, commonly used to represent solid shapes in computer graphics and computational mechanics.

2.2 Simplicial mappings

A simplicial mapping $f : \mathcal{M} \rightarrow \mathbb{R}^3$ is a particular piecewise affine mapping that satisfies its image $f(\mathcal{M})$ is also the underlying set of a simplicial 3-complex. The restriction mapping $f|_\tau$ on a tetrahedron $\tau = [v_i, v_j, v_k, v_\ell] \in \mathbb{T}(\mathcal{M})$ is formulated as

$$f|_\tau(v) = \frac{1}{|\tau|} \left(\lambda_i(\tau, v) f(v_i) + \lambda_j(\tau, v) f(v_j) + \lambda_k(\tau, v) f(v_k) + \lambda_\ell(\tau, v) f(v_\ell) \right),$$

where the signed volume $|\tau| = |[v_i, v_j, v_k, v_\ell]|$ is defined as

$$|[v_i, v_j, v_k, v_\ell]| = \frac{1}{6} \left(((v_j - v_i) \times (v_k - v_i))^\top (v_\ell - v_i) \right),$$

the coefficients $\lambda_i(\tau, v) = \frac{|[v, v_j, v_k, v_\ell]|}{|\tau|}$, $\lambda_j(\tau, v) = \frac{|[v_i, v, v_k, v_\ell]|}{|\tau|}$, $\lambda_k(\tau, v) = \frac{|[v_i, v_j, v, v_\ell]|}{|\tau|}$ and $\lambda_\ell(\tau, v) = \frac{|[v_i, v_j, v_k, v]|}{|\tau|}$ are called the barycentric coordinates on the tetrahedron τ . In practice, a simplicial mapping f is represented as a matrix

$$\mathbf{f} = \begin{bmatrix} f(v_1)^\top \\ \vdots \\ f(v_n)^\top \end{bmatrix} = \begin{bmatrix} f_1^\top \\ \vdots \\ f_n^\top \end{bmatrix} = \begin{bmatrix} f_1^1 & f_1^2 & f_1^3 \\ \vdots & \vdots & \vdots \\ f_n^1 & f_n^2 & f_n^3 \end{bmatrix} = [\mathbf{f}^1 \quad \mathbf{f}^2 \quad \mathbf{f}^3] \in \mathbb{R}^{n \times 3}. \quad (1)$$

A simplicial mapping f is said to be volume-preserving if the volume of each transformed tetrahedron is equal to the original one up to a global constant scaling factor $c \in \mathbb{R}$, i.e., $|f(\tau)| = c|\tau|$, for some $c \in \mathbb{R}$, for all $\tau \in \mathbb{T}(\mathcal{M})$. The mapping f is orientation-preserving if $c > 0$, and orientation-reversing if $c < 0$. The mapping f is called a trivial mapping if $c = 0$. A desirable volume-preserving mapping is one with a nonzero scaling factor, i.e., a nontrivial or a bijective one.

2.3 Isovolumetric energy functional

In this paper, the adopted objective functional for computing volume-preserving parameterizations is the isovolumetric energy defined as

$$E_I(f) = \frac{\mathcal{V}(e)}{\mathcal{V}(f)} E_V(f) - \mathcal{V}(f), \quad (2a)$$

where \mathcal{V} denotes the image volume measurement, e denotes the identity mapping on \mathcal{M} , and E_V denotes the volumetric stretch energy functional [17] defined as

$$E_V(f) = \sum_{\tau \in \mathbb{T}(\mathcal{M})} \frac{|f(\tau)|^2}{|\tau|}. \quad (2b)$$

The definition of E_V in (2b) is equivalent to [17, (3.3)] with a scaling factor of 2/3.

It is proved in [17, Theorem 3.1] that $E_V(f)$ in (2b) can be represented as

$$E_V(f) = \frac{1}{2} \text{trace}(\mathbf{f}^\top L_V(f) \mathbf{f}) = \frac{1}{2} \sum_{s=1}^3 \mathbf{f}^{s\top} L_V(f) \mathbf{f}^s, \quad (3a)$$

where \mathbf{f} and \mathbf{f}^s are the matrix and vectors defined in (1), $L_V(f)$ is the weighted Laplacian matrix defined as

$$[L_V(f)]_{i,j} = \begin{cases} - \sum_{[v_i, v_j, v_k, v_\ell] \in \mathbb{T}(\mathcal{M})} [\omega_V(f)]_{i,j}^{k,\ell} & \text{if } [v_i, v_j] \in \mathbb{E}(\mathcal{M}), \\ - \sum_{[v_i, v_k] \in \mathbb{E}(\mathcal{M})} [L_V(f)]_{i,k} & \text{if } j = i, \\ 0 & \text{otherwise.} \end{cases} \quad (3b)$$

The mapping-dependent weight function $\omega_V(f)$ is the modified cotangent weight defined as

$$[\omega_V(f)]_{i,j}^{k,\ell} = \frac{\cot(\theta_{i,j}^{k,\ell}(f)) |f([v_i, v_j, v_k, v_\ell])|}{9 |[v_i, v_j, v_k, v_\ell]|}, \quad (3c)$$

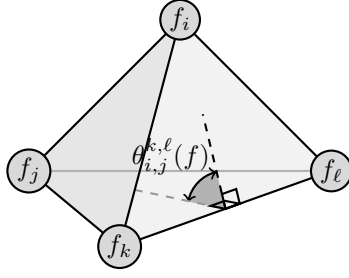


Figure 1: An illustration of the dihedral angle between faces $f([v_i, v_k, v_\ell])$ and $f([v_j, v_\ell, v_k])$ in the tetrahedron $f(\tau) = [f_i, f_j, f_k, f_\ell]$.

where $\theta_{i,j}^{k,\ell}(f)$ is the dihedral angle between triangular faces $f([v_i, v_k, v_\ell])$ and $f([v_j, v_\ell, v_k])$ in the tetrahedron $f(\tau) = [f_i, f_j, f_k, f_\ell]$ on the edge $f([v_k, v_\ell])$, as illustrated in Figure 1.

The volumetric stretch energy E_V in (3) was defined by Yueh et al. [28] for computing volume-preserving parameterizations of simplicial 3-manifolds. Under the constraint that the total volume of the manifold remains unchanged, Huang et al. [17] further proved that the lower bound of $E_V(f)$ is $\mathcal{V}(f)$. The equality holds if and only if the mapping f is volume-preserving [17, Theorem 3.3]. Based on this fact, it is natural to define the isovolumetric energy as the difference between $E_V(f)$ and $\mathcal{V}(f)$. To release the constraint $\mathcal{V}(f) = \mathcal{V}(e)$, we scale $E_V(f)$ by the factor $\mathcal{V}(e)/\mathcal{V}(f)$ in our proposed objective functional (2). In the following theorem, we derive an analogous consequence of [17, Theorem 3.3] without the constant total image volume assumption.

Theorem 1. *Let \mathcal{M} be a simplicial 3-manifold and f be a simplicial mapping defined on \mathcal{M} . The isovolumetric energy in (2) satisfies*

$$E_I(f) \geq 0,$$

and the equality holds if and only if f is volume-preserving.

Proof. By applying the Cauchy–Schwarz inequality to (2b), we have

$$E_V(f) \mathcal{V}(e) = \sum_{\tau \in \mathbb{T}(\mathcal{M})} \frac{|f(\tau)|^2}{|\tau|} \sum_{\tau \in \mathbb{T}(\mathcal{M})} |\tau| \geq \left(\sum_{\tau \in \mathbb{T}(\mathcal{M})} |f(\tau)| \right)^2 = \mathcal{V}(f)^2.$$

Divide both sides of the inequality by $\mathcal{V}(f)$, we obtain

$$\frac{\mathcal{V}(e)}{\mathcal{V}(f)} E_V(f) \geq \mathcal{V}(f),$$

i.e., the isovolumetric energy (2) satisfies $E_I(f) \geq 0$. The equality holds if and only if $\frac{|f(\tau)|}{|\tau|}$ is constant, i.e., f is volume-preserving. \square

Theorem 1 provides a robust foundation for computing volume-preserving parameterizations by minimizing the isovolumetric energy (2). Especially when the boundary vertices are allowed to glide along the unit sphere, the exact image volume is not constant.

3 IEM for ball-shaped parameterizations

Recall that a ball-shaped parameterization of a simplicial 3-manifold is a bijective mapping with boundary vertices being mapped to the unit sphere. To remove the spherical constraint for boundary vertices in the objective functional (2), we represent the boundary mapping in spherical coordinates. We denote the index sets of boundary and interior vertices as

$$\mathbf{B} = \{b \mid v_b \in \partial\mathcal{M}\} \quad \text{and} \quad \mathbf{I} = \{i \mid v_i \in \mathcal{M} \setminus \partial\mathcal{M}\},$$

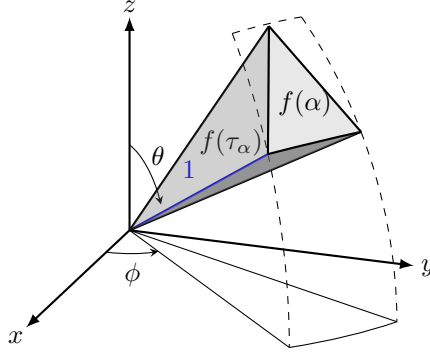


Figure 2: An illustration for the tetrahedron $f(\tau_\alpha)$ formed by the boundary face $f(\alpha)$ and the origin \mathbf{O}_3 of \mathbb{R}^3 .

respectively. Then, the boundary mapping $\mathbf{f}_B = (\mathbf{f}_B^1, \mathbf{f}_B^2, \mathbf{f}_B^3)$ can be represented in spherical coordinates as

$$\mathbf{f}_B^1 = \sin \boldsymbol{\theta} \odot \cos \boldsymbol{\phi}, \quad \mathbf{f}_B^2 = \sin \boldsymbol{\theta} \odot \sin \boldsymbol{\phi}, \quad \text{and} \quad \mathbf{f}_B^3 = \cos \boldsymbol{\theta}, \quad (4)$$

where $\boldsymbol{\theta} = (\theta_1, \dots, \theta_{n_B})^\top \in \mathbb{R}^{n_B}$ and $\boldsymbol{\phi} = (\phi_1, \dots, \phi_{n_B})^\top \in \mathbb{R}^{n_B}$. Conversely, spherical coordinates $(\boldsymbol{\theta}, \boldsymbol{\phi})$ can be represented by $\mathbf{f}_B = (\mathbf{f}_B^1, \mathbf{f}_B^2, \mathbf{f}_B^3)$ as

$$\boldsymbol{\theta} = \arccos(\mathbf{f}_B^3), \quad \boldsymbol{\phi} = \text{atan2}(\mathbf{f}_B^2, \mathbf{f}_B^1), \quad (5)$$

where atan2 denotes the four-quadrant inverse tangent. First, we reformulate the image volume $\mathcal{V}(f)$ in (2) in spherical coordinates $\boldsymbol{\theta}$ and $\boldsymbol{\phi}$. Let $\alpha = [v_i, v_j, v_k] \in \mathbb{F}(\partial\mathcal{M})$ be a boundary triangular face. We denote

$$f(\tau_\alpha) = [\mathbf{O}_3, f(\alpha)] = [\mathbf{O}_3, \mathbf{f}_i, \mathbf{f}_j, \mathbf{f}_k]$$

as the tetrahedron formed by the image of boundary face $f(\alpha)$ together with the origin \mathbf{O}_3 of \mathbb{R}^3 . The image volume of f can be represented as

$$\mathcal{V}(f) = \sum_{\alpha \in \mathbb{F}(\partial\mathcal{M})} |f(\tau_\alpha)| = \frac{1}{6} \sum_{[v_i, v_j, v_k] \in \mathbb{F}(\partial\mathcal{M})} \mathbf{f}_i^\top (\mathbf{f}_j \times \mathbf{f}_k),$$

as illustrated in Figure 2.

We denote the vertex coordinates of the boundary face $\alpha = [v_i, v_j, v_k]$ on the image $f(\alpha)$ as $\mathbf{f}_\alpha^s = (f_i^s, f_j^s, f_k^s)^\top$, for $s = 1, 2, 3$. Now we represent $\mathbf{f}_\alpha^1, \mathbf{f}_\alpha^2, \mathbf{f}_\alpha^3$ in spherical coordinates $\boldsymbol{\theta}_\alpha = (\theta_i, \theta_j, \theta_k)^\top$ and $\boldsymbol{\phi}_\alpha = (\phi_i, \phi_j, \phi_k)^\top$ as

$$\begin{aligned} \mathbf{f}_\alpha^1 &= \begin{bmatrix} \sin \theta_i \cos \phi_i \\ \sin \theta_j \cos \phi_j \\ \sin \theta_k \cos \phi_k \end{bmatrix} = \begin{bmatrix} \sin \theta_i \\ \sin \theta_j \\ \sin \theta_k \end{bmatrix} \odot \begin{bmatrix} \cos \phi_i \\ \cos \phi_j \\ \cos \phi_k \end{bmatrix} =: \sin \boldsymbol{\theta}_\alpha \odot \cos \boldsymbol{\phi}_\alpha, \\ \mathbf{f}_\alpha^2 &= \begin{bmatrix} \sin \theta_i \sin \phi_i \\ \sin \theta_j \sin \phi_j \\ \sin \theta_k \sin \phi_k \end{bmatrix} = \begin{bmatrix} \sin \theta_i \\ \sin \theta_j \\ \sin \theta_k \end{bmatrix} \odot \begin{bmatrix} \sin \phi_i \\ \sin \phi_j \\ \sin \phi_k \end{bmatrix} =: \sin \boldsymbol{\theta}_\alpha \odot \sin \boldsymbol{\phi}_\alpha, \\ \mathbf{f}_\alpha^3 &= \begin{bmatrix} \cos \theta_i \\ \cos \theta_j \\ \cos \theta_k \end{bmatrix} = \cos \boldsymbol{\theta}_\alpha, \end{aligned}$$

where \odot denotes the Hadamard product of matrices or vectors. Ultimately, the problem of IEM for ball-shaped parameterizations can be formulated as

$$f^* = \underset{\substack{\mathbf{f}_I^1, \mathbf{f}_I^2, \mathbf{f}_I^3 \in \mathbb{R}^{n_I} \\ \boldsymbol{\theta}, \boldsymbol{\phi} \in \mathbb{R}^{n_B}}}{\text{argmin}} E_I(\mathbf{f}_I^1, \mathbf{f}_I^2, \mathbf{f}_I^3, \boldsymbol{\theta}, \boldsymbol{\phi}). \quad (6)$$

The gradient of the image volume $|f(\tau_\alpha)|$ with respect to $\mathbf{f}_\alpha^1, \mathbf{f}_\alpha^2, \mathbf{f}_\alpha^3$ can be formulated as

$$\nabla_{\mathbf{f}_\alpha^1}|f(\tau_\alpha)| = \frac{1}{6}(\mathbf{f}_\alpha^2 \times \mathbf{f}_\alpha^3), \quad \nabla_{\mathbf{f}_\alpha^2}|f(\tau_\alpha)| = \frac{1}{6}(\mathbf{f}_\alpha^3 \times \mathbf{f}_\alpha^1), \quad \nabla_{\mathbf{f}_\alpha^3}|f(\tau_\alpha)| = \frac{1}{6}(\mathbf{f}_\alpha^1 \times \mathbf{f}_\alpha^2).$$

By applying the chain rule, the gradient of $|f(\tau_\alpha)|$ with respect to $\boldsymbol{\theta}_\alpha$ and $\boldsymbol{\phi}_\alpha$ can be formulated as

$$\nabla_{\boldsymbol{\theta}_\alpha}|f(\tau_\alpha)| = \frac{1}{6}(\cos \boldsymbol{\theta}_\alpha \odot \cos \boldsymbol{\phi}_\alpha \odot (\mathbf{f}_\alpha^2 \times \mathbf{f}_\alpha^3) + \cos \boldsymbol{\theta}_\alpha \odot \sin \boldsymbol{\phi}_\alpha \odot (\mathbf{f}_\alpha^3 \times \mathbf{f}_\alpha^1) - \sin \boldsymbol{\theta}_\alpha \odot (\mathbf{f}_\alpha^1 \times \mathbf{f}_\alpha^2)), \quad (7a)$$

$$\nabla_{\boldsymbol{\phi}_\alpha}|f(\tau_\alpha)| = \frac{1}{6}(\sin \boldsymbol{\theta}_\alpha \odot \cos \boldsymbol{\phi}_\alpha \odot (\mathbf{f}_\alpha^3 \times \mathbf{f}_\alpha^1) - \sin \boldsymbol{\theta}_\alpha \odot \sin \boldsymbol{\phi}_\alpha \odot (\mathbf{f}_\alpha^2 \times \mathbf{f}_\alpha^3)). \quad (7b)$$

We denote the gradient of $\mathcal{V}(f)$ with respect to $\boldsymbol{\theta}$ and $\boldsymbol{\phi}$ as $\nabla_{\boldsymbol{\theta}}\mathcal{V}(f)$ and $\nabla_{\boldsymbol{\phi}}\mathcal{V}(f)$, respectively, which can be obtained by assembling associated tetrahedra using the formulae in (7).

On the other hand, from [17, Theorem 3.5], the gradient of $E_V(f)$ with respect to \mathbf{f}^s is formulated as

$$\nabla_{\mathbf{f}^s} E_V(f) = 3 L_V(f) \mathbf{f}^s, \quad \text{for } s = 1, 2, 3. \quad (8)$$

Under a reordering with respect to I and B, the gradient formula (8) is equivalent to

$$\nabla_{\mathbf{f}_I^s} E_V(f) = 3 ([L_V(f)]_{I,I} \mathbf{f}_I^s + [L_V(f)]_{I,B} \mathbf{f}_B^s), \quad (9a)$$

$$\nabla_{\mathbf{f}_B^s} E_V(f) = 3 ([L_V(f)]_{B,I} \mathbf{f}_I^s + [L_V(f)]_{B,B} \mathbf{f}_B^s), \quad \text{for } s = 1, 2, 3. \quad (9b)$$

By applying the chain rule, the gradient of $E_I(f)$ with respect to $\mathbf{f}_I^s, \boldsymbol{\theta}$, and $\boldsymbol{\phi}$ can be formulated as

$$\begin{aligned} \nabla_{\mathbf{f}_I^s} E_I(f) &= \left(\frac{\mathcal{V}(e)}{2\mathcal{V}(f)} \right) \nabla_{\mathbf{f}_I^s} (\text{trace}(\mathbf{f}^\top L_V(f) \mathbf{f})) \\ &= \left(\frac{3\mathcal{V}(e)}{\mathcal{V}(f)} \right) ([L_V(f)]_{I,I} \mathbf{f}_I^s + [L_V(f)]_{I,B} \mathbf{f}_B^s), \quad \text{for } s = 1, 2, 3, \end{aligned} \quad (10a)$$

$$\begin{aligned} \nabla_{\boldsymbol{\theta}} E_I(f) &= \nabla_{\boldsymbol{\theta}} \left(\frac{\mathcal{V}(e)}{2\mathcal{V}(f)} \right) (\text{trace}(\mathbf{f}^\top L_V(f) \mathbf{f})) + \left(\frac{\mathcal{V}(e)}{2\mathcal{V}(f)} \right) \nabla_{\boldsymbol{\theta}} (\text{trace}(\mathbf{f}^\top L_V(f) \mathbf{f})) - \nabla_{\boldsymbol{\theta}} (\mathcal{V}(f)) \\ &= \left(\frac{3\mathcal{V}(e)}{\mathcal{V}(f)} \right) \left(\cos \boldsymbol{\theta} \odot \cos \boldsymbol{\phi} \odot ([L_V(f)]_{B,I} \mathbf{f}_I^1 + [L_V(f)]_{B,B} \mathbf{f}_B^1) \right. \\ &\quad \left. + \cos \boldsymbol{\theta} \odot \sin \boldsymbol{\phi} \odot ([L_V(f)]_{B,I} \mathbf{f}_I^2 + [L_V(f)]_{B,B} \mathbf{f}_B^2) \right. \\ &\quad \left. - \sin \boldsymbol{\theta} \odot ([L_V(f)]_{B,I} \mathbf{f}_I^3 + [L_V(f)]_{B,B} \mathbf{f}_B^3) \right) \\ &\quad - \left(1 + \frac{\mathcal{V}(e) \text{trace}(\mathbf{f}^\top L_V(f) \mathbf{f})}{2(\mathcal{V}(f))^2} \right) \nabla_{\boldsymbol{\theta}} (\mathcal{V}(f)), \end{aligned} \quad (10b)$$

and

$$\begin{aligned} \nabla_{\boldsymbol{\phi}} E_I(f) &= \nabla_{\boldsymbol{\phi}} \left(\frac{\mathcal{V}(e)}{2\mathcal{V}(f)} \right) (\text{trace}(\mathbf{f}^\top L_V(f) \mathbf{f})) + \left(\frac{\mathcal{V}(e)}{2\mathcal{V}(f)} \right) \nabla_{\boldsymbol{\phi}} (\text{trace}(\mathbf{f}^\top L_V(f) \mathbf{f})) - \nabla_{\boldsymbol{\phi}} (\mathcal{V}(f)) \\ &= \left(\frac{3\mathcal{V}(e)}{\mathcal{V}(f)} \right) \left(\sin \boldsymbol{\theta} \odot \cos \boldsymbol{\phi} \odot ([L_V(f)]_{B,I} \mathbf{f}_I^2 + [L_V(f)]_{B,B} \mathbf{f}_B^2) \right. \\ &\quad \left. - \sin \boldsymbol{\theta} \odot \sin \boldsymbol{\phi} \odot ([L_V(f)]_{B,I} \mathbf{f}_I^1 + [L_V(f)]_{B,B} \mathbf{f}_B^1) \right) \\ &\quad - \left(1 + \frac{\mathcal{V}(e) \text{trace}(\mathbf{f}^\top L_V(f) \mathbf{f})}{2(\mathcal{V}(f))^2} \right) \nabla_{\boldsymbol{\phi}} (\mathcal{V}(f)). \end{aligned} \quad (10c)$$

Based on the explicit gradient formulae of E_I in (10), we develop the preconditioned nonlinear CG method for solving the problem (6), which is introduced in detail in the next section.

4 Preconditioned nonlinear CG method of IEM

Now we demonstrate the preconditioned nonlinear CG method of IEM for ball-shaped volume-preserving parameterizations.

Note that the target shape is a solid unit ball. To achieve a better mapping, it is natural to perform an anisotropic scaling transformation (AST) to normalize the bounding box of the mesh model before the ball-shaped mapping. Let

$$\mathbf{v} = \begin{bmatrix} v_1^1 & v_1^2 & v_1^3 \\ \vdots & \vdots & \vdots \\ v_n^1 & v_n^2 & v_n^3 \end{bmatrix}$$

be the matrix representation of vertex set $\mathbb{V}(\mathcal{M})$ and $\mathbf{c} = \frac{1}{n} \mathbf{v}^\top \mathbf{1}_n$ be the center of the vertices. The AST $T_a : \mathbb{R}^3 \rightarrow \mathbb{R}^3$ is formulated as

$$T_a(\mathbf{x}) = \begin{bmatrix} r_1 & & \\ & r_2 & \\ & & r_3 \end{bmatrix} R(\mathbf{x} - \mathbf{c}), \quad (11)$$

where $R \in \text{SO}(3)$ is a suitable rotation and $r_\ell = 1/\max_{1 \leq s \leq n} [R(v_s - \mathbf{c})]_\ell$, for $\ell = 1, 2, 3$. The matrix R is chosen to rotate the principal components to the standard Euclidean frame. Let

$$P = \mathbf{v} - \mathbf{1}_n \mathbf{c}^\top \in \mathbb{R}^{n \times 3} \quad (12)$$

be the matrix representation of centralized vertices. Each row of P is a centralized vertex. The rotation matrix is computed by the singular value decomposition (SVD)

$$P = U \Sigma V^\top. \quad (13)$$

The rotation matrix in (11) is then given by $R = V^\top$.

In practice, the initial mapping $f^{(0)}$ is computed by the fixed-point method of the VSEM in [28, Algorithm 4.4] with a few iteration steps, e.g., 15 steps. At the k th iteration step, we represent the mapping $f^{(k)}$ by

$$\widehat{\mathbf{f}}^{(k)} = \begin{bmatrix} \mathbf{f}_I^{1(k)} \\ \mathbf{f}_I^{2(k)} \\ \mathbf{f}_I^{3(k)} \\ \boldsymbol{\theta}^{(k)} \\ \phi^{(k)} \end{bmatrix}. \quad (14)$$

The corresponding gradient vector

$$\widehat{\mathbf{g}}^{(k)} := \nabla E_I(\widehat{\mathbf{f}}^{(k)}) = \begin{bmatrix} \nabla_{\mathbf{f}_I^1} E_I(f^{(k)}) \\ \nabla_{\mathbf{f}_I^2} E_I(f^{(k)}) \\ \nabla_{\mathbf{f}_I^3} E_I(f^{(k)}) \\ \nabla_{\boldsymbol{\theta}} E_I(f^{(k)}) \\ \nabla_{\phi} E_I(f^{(k)}) \end{bmatrix} =: \begin{bmatrix} \mathbf{g}_I^{1(k)} \\ \mathbf{g}_I^{2(k)} \\ \mathbf{g}_I^{3(k)} \\ \mathbf{g}_{\boldsymbol{\theta}}^{(k)} \\ \mathbf{g}_{\phi}^{(k)} \end{bmatrix} \quad (15)$$

is explicitly formulated in (10). For $k \geq 1$, we update the interior and boundary mappings along the CG directions with the step length α_k as

$$\widehat{\mathbf{f}}^{(k+1)} = \widehat{\mathbf{f}}^{(k)} + \alpha_k \widehat{\mathbf{p}}^{(k)}, \quad (16a)$$

where $\widehat{\mathbf{p}}^{(k)}$ is the CG direction at k th step given by

$$\widehat{\mathbf{p}}^{(k)} = \begin{bmatrix} \mathbf{p}_I^{1(k)} \\ \mathbf{p}_I^{2(k)} \\ \mathbf{p}_I^{3(k)} \\ \mathbf{p}_{\boldsymbol{\theta}}^{(k)} \\ \mathbf{p}_{\phi}^{(k)} \end{bmatrix} = -M^{-1} \widehat{\mathbf{g}}^{(k)} + \beta_k \widehat{\mathbf{p}}^{(k-1)}. \quad (16b)$$

provided that $\widehat{\mathbf{p}}^{(0)} = -M^{-1}\widehat{\mathbf{g}}^{(0)}$ and the corrective scalar

$$\beta_k = \frac{\widehat{\mathbf{g}}^{(k)\top} M^{-1} \widehat{\mathbf{g}}^{(k)}}{\widehat{\mathbf{g}}^{(k-1)\top} M^{-1} \widehat{\mathbf{g}}^{(k-1)}} \quad (16c)$$

with the preconditioner

$$M = \begin{bmatrix} I_3 \otimes [L_V(f^{(0)})]_{\mathbf{I},\mathbf{I}} & \\ & I_2 \otimes [L_V(f^{(0)})]_{\mathbf{B},\mathbf{B}} \end{bmatrix}.$$

In practice, we computed the preordered Cholesky decomposition so that linear systems of $[L_V(f^{(0)})]_{\mathbf{I},\mathbf{I}}$ and $[L_V(f^{(0)})]_{\mathbf{B},\mathbf{B}}$ can be efficiently solved by forward and backward substitutions.

To estimate the optimal step length α_k , we define $\Phi^{(k)}(\alpha) : \mathbb{R} \rightarrow \mathbb{R}$ as

$$\Phi^{(k)}(\alpha) = E_I(\widehat{\mathbf{f}}^{(k)} + \alpha \widehat{\mathbf{p}}^{(k)}),$$

It is desirable to choose the minimizer α_k of $\Phi^{(k)}$ that satisfies $\nabla \Phi^{(k)}(\alpha_k) = 0$ as the step lengths. However, it is not feasible due to the nonlinearity of the Laplacian matrix (3b). Instead, we approximate $\Phi^{(k)}$ by a quadratic function $\Phi_q^{(k)}$ as

$$\Phi_q^{(k)}(\alpha) = a_k \alpha^2 + b_k \alpha + c_k,$$

which satisfies

$$\begin{cases} \Phi_q^{(k)}(0) = \Phi^{(k)}(0) = E_I(\widehat{\mathbf{f}}^{(k)}), \\ \frac{d}{d\alpha} \Phi_q^{(k)}(0) = \frac{d}{d\alpha} \Phi^{(k)}(0) = \mathbf{p}^{(k)\top} \nabla E_I(\widehat{\mathbf{f}}^{(k)}), \\ \Phi_q^{(k)}(\alpha_{k-1}) = \Phi^{(k)}(\alpha_{k-1}) = E_I(\widehat{\mathbf{f}}^{(k)} + \alpha_{k-1} \widehat{\mathbf{p}}^{(k)}). \end{cases}$$

The coefficients a_k , b_k , and c_k are thus can be computed by

$$\begin{aligned} a_k &= \Phi^{(k)}(0), \quad b_k = \frac{d}{d\alpha} \Phi^{(k)}(0), \quad \text{and} \\ c_k &= \frac{1}{\alpha_{k-1}^2} \left(\Phi^{(k)}(\alpha_{k-1}) - \Phi^{(k)}(0) - \alpha_{k-1} \frac{d}{d\alpha} \Phi^{(k)}(0) \right). \end{aligned}$$

As a result, we approximate the minimizer of $\Phi^{(k)}(\alpha)$ by the minimizer of $\Phi_q^{(k)}(\alpha)$ as

$$\alpha_k = \frac{-\frac{d}{d\alpha} \Phi^{(k)}(0)}{2a_k} = \frac{-\alpha_{k-1}^2 \frac{d}{d\alpha} \Phi^{(k)}(0)}{2(\Phi^{(k)}(\alpha_{k-1}) - \Phi^{(k)}(0) - \alpha_{k-1} \frac{d}{d\alpha} \Phi^{(k)}(0))}. \quad (17)$$

The detailed computational procedure is summarized in Algorithm 1.

5 Convergence analysis of IEM algorithm

In this section, we provide the proof in detail for the global convergence of the proposed IEM, Algorithm 1. The consequence of the main theorem (Theorem 2) is a generalization of the convergence of the nonlinear CG method introduced in [22, Chapter 5]. Similar techniques have been applied in the convergence analysis of the authalic energy minimization for disk area-preserving parameterizations [21]. One of the main differences is that we change the definition of the denominator of $\cos \theta_M^{(k)}$ in the modified Zoutendijk's condition (Lemma 4) so that the proof of Theorem 2 would be simpler. For simplicity, in the remaining part of this section, we denote $\widehat{\mathbf{f}}$ in (14), $\widehat{\mathbf{g}}$ in (15), and $\widehat{\mathbf{p}}$ in (16b) as \mathbf{f} , \mathbf{g} , and \mathbf{p} , respectively.

The global convergence of Algorithm 1 is theoretically guaranteed under the assumption that each step length α_k satisfies the strong Wolfe conditions

$$E_I(\mathbf{f}^{(k)} + \alpha_k \mathbf{p}^{(k)}) \leq E_I(\mathbf{f}^{(k)}) + c_1 \alpha_k \nabla E_I(\mathbf{f}^{(k)})^\top \mathbf{p}^{(k)}, \quad (18a)$$

$$|\nabla E_I(\mathbf{f}^{(k)} + \alpha_k \mathbf{p}^{(k)})^\top \mathbf{p}^{(k)}| \leq c_2 |\nabla E_I(\mathbf{f}^{(k)})^\top \mathbf{p}^{(k)}|, \quad (18b)$$

with $0 < c_1 < c_2 < \frac{1}{2}$. The existence of each desirable step length α_k is guaranteed by Lemma 2 under the assumption that $\mathbf{p}^{(k)}$ is a descent direction of E_I at $\mathbf{f}^{(k)}$.

In the following lemma, we prove the Lipschitz continuities of the objective functional and its gradient with respect to the vertex image, which play crucial roles in the proof of the convergence of IEM.

Algorithm 1 Preconditioned Nonlinear CG Method for IEM

Input: A simply connected tetrahedral mesh \mathcal{M} , a tolerance ϵ .

Output: A volume-preserving simplicial mapping f .

- 1: Let P be the centralized vertices as in (12).
 - 2: Compute the SVD $P = U\Sigma V^\top$ as in (13).
 - 3: Perform AST to all vertices by $v_s \leftarrow T_a(v_s)$ as in (11).
 - 4: Let n be the number of vertices of \mathcal{M} .
 - 5: Let $\mathbf{B} = \{s \mid v_s \in \partial\mathcal{M}\}$ and $\mathbf{I} = \{1, \dots, n\} \setminus \mathbf{B}$.
 - 6: Compute spherical area-preserving boundary map $\mathbf{f}_{\mathbf{B}}$ by [28, Algorithm 4.3].
 - 7: Let $L \leftarrow L_V(e)$ as (3b).
 - 8: Solve the linear system $L_{\mathbf{I},\mathbf{I}}\mathbf{f}_{\mathbf{I}} = -L_{\mathbf{I},\mathbf{B}}\mathbf{f}_{\mathbf{B}}$.
 - 9: **for** $k = 1, \dots, 15$ **do**
 - 10: Update $L \leftarrow L_V(f)$ as (3b).
 - 11: Solve the linear system $L_{\mathbf{I},\mathbf{I}}\mathbf{f}_{\mathbf{I}} = -L_{\mathbf{I},\mathbf{B}}\mathbf{f}_{\mathbf{B}}$.
 - 12: **end for**
 - 13: Update $L \leftarrow L_V(f)$ as (3b).
 - 14: Compute the energy value $E = E_1(f)$ as (2).
 - 15: Let preconditioners $M_{\mathbf{I}} \leftarrow L_{\mathbf{I},\mathbf{I}}$ and $M_{\mathbf{B}} \leftarrow L_{\mathbf{B},\mathbf{B}}$.
 - 16: Perform Cholesky decompositions of $M_{\mathbf{I}}$ and $M_{\mathbf{B}}$.
 - 17: Compute spherical coordinates $[\boldsymbol{\theta}, \boldsymbol{\phi}]$ by (4).
 - 18: Let $\delta \leftarrow \infty$.
 - 19: **while** $\delta > \epsilon$ **do**
 - 20: Let $E_0 \leftarrow E$.
 - 21: Compute gradients $\mathbf{g}_{\mathbf{I}}, \mathbf{g}_{\boldsymbol{\theta}}, \mathbf{g}_{\boldsymbol{\phi}}$ by (10).
 - 22: Solve $M_{\mathbf{I}}\mathbf{h}_{\mathbf{I}} = \mathbf{g}_{\mathbf{I}}, M_{\mathbf{B}}\mathbf{h}_{\boldsymbol{\theta}} = \mathbf{g}_{\boldsymbol{\theta}}$ and $M_{\mathbf{B}}\mathbf{h}_{\boldsymbol{\phi}} = \mathbf{g}_{\boldsymbol{\phi}}$ by precomputed Cholesky decompositions.
 - 23: **if** $\delta = \infty$ **then**
 - 24: Compute $\lambda \leftarrow \text{trace}(\mathbf{g}_{\mathbf{I}}^\top \mathbf{h}_{\mathbf{I}}) + \mathbf{g}_{\boldsymbol{\theta}}^\top \mathbf{h}_{\boldsymbol{\theta}} + \mathbf{g}_{\boldsymbol{\phi}}^\top \mathbf{h}_{\boldsymbol{\phi}}$.
 - 25: Update $\mathbf{p}_{\mathbf{I}} \leftarrow -\mathbf{h}_{\mathbf{I}}, \mathbf{p}_{\boldsymbol{\theta}} \leftarrow -\mathbf{h}_{\boldsymbol{\theta}}$ and $\mathbf{p}_{\boldsymbol{\phi}} \leftarrow -\mathbf{h}_{\boldsymbol{\phi}}$.
 - 26: **else**
 - 27: Let $\lambda_0 \leftarrow \lambda$.
 - 28: Compute $\lambda \leftarrow \text{trace}(\mathbf{g}_{\mathbf{I}}^\top \mathbf{h}_{\mathbf{I}}) + \mathbf{g}_{\boldsymbol{\theta}}^\top \mathbf{h}_{\boldsymbol{\theta}} + \mathbf{g}_{\boldsymbol{\phi}}^\top \mathbf{h}_{\boldsymbol{\phi}}$.
 - 29: Let $\beta \leftarrow \lambda/\lambda_0$.
 - 30: Update $\mathbf{p}_{\mathbf{I}} \leftarrow -\mathbf{h}_{\mathbf{I}} + \beta\mathbf{p}_{\mathbf{I}}, \mathbf{p}_{\boldsymbol{\theta}} \leftarrow -\mathbf{h}_{\boldsymbol{\theta}} + \beta\mathbf{p}_{\boldsymbol{\theta}}$ and $\mathbf{p}_{\boldsymbol{\phi}} \leftarrow -\mathbf{h}_{\boldsymbol{\phi}} + \beta\mathbf{p}_{\boldsymbol{\phi}}$.
 - 31: **end if**
 - 32: Compute step length α by (17).
 - 33: Update $\mathbf{f}_{\mathbf{I}} \leftarrow \mathbf{f}_{\mathbf{I}} + \alpha\mathbf{p}_{\mathbf{I}}, \boldsymbol{\theta} \leftarrow \boldsymbol{\theta} + \alpha\mathbf{p}_{\boldsymbol{\theta}}$ and $\boldsymbol{\phi} \leftarrow \boldsymbol{\phi} + \alpha\mathbf{p}_{\boldsymbol{\phi}}$.
 - 34: Update $\mathbf{f}_{\mathbf{B}}$ by the inverse spherical coordinates of $(\boldsymbol{\theta}, \boldsymbol{\phi})$ as (5).
 - 35: Update $L \leftarrow L_V(f)$ as (3b).
 - 36: Compute the energy value $E = E_1(f)$ as (2).
 - 37: Update $\delta \leftarrow E_0 - E$.
 - 38: **end while**
-

Lemma 1. *The isovolumetric energy E_I (2) and its gradient ∇E_I are Lipschitz continuous.*

Proof. Similar to the matrix representation \mathbf{f} of a simplicial mapping f in (1), it can also be represented as a vector $(\mathbf{f}^{1\top}, \mathbf{f}^{2\top}, \mathbf{f}^{3\top})^\top$ of length $3n$, provided that n is the number of vertices of the triangular mesh model. The objective functional E_I of ball-shaped simplicial mapping can then be represented a function $E_I : [-1, 1]^{3n} \rightarrow \mathbb{R}$ defined on a compact subset $[-1, 1]^{3n}$ of \mathbb{R}^{3n} as

$$E_I(f) \equiv E_I(\mathbf{f}) \equiv E_I(f_1^1, \dots, f_n^1, f_1^2, \dots, f_n^2, f_1^3, \dots, f_n^3).$$

Then, for every ball-shaped simplicial mappings \mathbf{x} and $\mathbf{y} \in [-1, 1]^{3n}$, we define $\phi(t) = E_I((1-t)\mathbf{x} + t\mathbf{y})$. Since E_I is smooth, by the mean value theorem, there exists a value $\xi_1 \in (0, 1)$ such that $\mathbf{z}_1 = (1 - \xi_1)\mathbf{x} + \xi_1\mathbf{y}$ and

$$E_I(\mathbf{y}) - E_I(\mathbf{x}) = \phi(1) - \phi(0) = \phi'(\xi_1) = \nabla E_I(\mathbf{z}_1)^\top (\mathbf{y} - \mathbf{x}).$$

Since the domain of E_I is compact,

$$\|E_I(\mathbf{y}) - E_I(\mathbf{x})\| \leq C_1 \|\mathbf{y} - \mathbf{x}\|,$$

where $C_1 = \max_{\mathbf{f} \in [-1, 1]^{3n}} \|\nabla E_I(\mathbf{f})\|$ is finite, i.e., E_I is Lipschitz continuous.

On the other hand, to show the Lipschitz continuity of ∇E_I , we define $\varphi(t) = (\nabla E_I(\mathbf{y}) - \nabla E_I(\mathbf{x}))^\top \nabla E_I((1-t)\mathbf{x} + t\mathbf{y})$. Since ∇E_I is smooth, by the mean value theorem, there exists a value $\xi_2 \in (0, 1)$ such that $\mathbf{z}_2 = (1 - \xi_2)\mathbf{x} + \xi_2\mathbf{y}$ and

$$\begin{aligned} \|\nabla E_I(\mathbf{y}) - \nabla E_I(\mathbf{x})\|^2 &= \varphi(1) - \varphi(0) = \varphi'(\xi_2) \\ &= (\nabla E_I(\mathbf{y}) - \nabla E_I(\mathbf{x}))^\top \nabla^2 E_I(\mathbf{z}_2) (\mathbf{y} - \mathbf{x}). \end{aligned}$$

Since the domain of E_I is compact,

$$\|\nabla E_I(\mathbf{y}) - \nabla E_I(\mathbf{x})\|^2 \leq C_2 \|\nabla E_I(\mathbf{y}) - \nabla E_I(\mathbf{x})\| \|\mathbf{y} - \mathbf{x}\|,$$

where $C_2 = \max_{\mathbf{f} \in [-1, 1]^{3n}} \|\nabla^2 E_I(\mathbf{f})\|$ is finite, i.e., ∇E_I is Lipschitz continuous. \square

To guarantee the energy E_I decreases sufficiently at the k th iteration step, we require not only the descent direction $\mathbf{p}^{(k)}$, but also a proper step length α_k that satisfies the strong Wolfe conditions (18). Since E_I is bounded below, the following lemma guarantees the existence of such desirable step lengths.

Lemma 2 ([22, Lemma 3.1]). *Intervals of step lengths that satisfy the strong Wolfe conditions (18) always exist, provided that $0 < c_1 < c_2 < 1$ and $\mathbf{p}^{(k)}$ is a descent direction at $\mathbf{f}^{(k)}$.*

For $k = 0$, since M^{-1} is symmetric positive definite, $\mathbf{p}^{(0)} = -M^{-1}\mathbf{g}^{(0)}$ is a descent direction, and thus the existence of a desirable step length $\alpha^{(0)}$ satisfying (18) is guaranteed by Lemma 2. To keep $\mathbf{p}^{(k)}$ being the descent direction for $k \geq 1$, the constant c_2 should be chosen in $(0, \frac{1}{2})$. The following lemma, a variant of [22, Lemma 5.6], provides crucial bounds of the value $\frac{\nabla E_I(\mathbf{f}^{(k)})^\top \mathbf{p}^{(k)}}{\|\nabla E_I(\mathbf{f}^{(k)})\|_{M^{-1}}^2}$, which serves as a core step for the proof of the global convergence of the IEM.

Lemma 3. *Let M be a symmetric positive definite matrix. Suppose the step length α_k satisfies the strong Wolfe conditions (18). Then, the vector $\mathbf{p}^{(k)}$ satisfies*

$$-\frac{1}{1 - c_2} \leq \frac{\nabla E_I(\mathbf{f}^{(k)})^\top \mathbf{p}^{(k)}}{\|\nabla E_I(\mathbf{f}^{(k)})\|_{M^{-1}}^2} \leq \frac{2c_2 - 1}{1 - c_2}, \quad (19)$$

for all $k \geq 0$, where $\|\cdot\|_{M^{-1}}$ denotes the M^{-1} -norm defined as $\|\mathbf{v}\|_{M^{-1}} = \sqrt{\mathbf{v}^\top M^{-1} \mathbf{v}}$.

Proof. We prove (19) by induction on k . For $k = 0$, since $\mathbf{p}^{(0)} = -M^{-1}\mathbf{g}^{(0)}$, we have

$$\frac{\nabla E_I(\mathbf{f}^{(0)})^\top \mathbf{p}^{(0)}}{\|\nabla E_I(\mathbf{f}^{(0)})\|_{M^{-1}}^2} = \frac{-\mathbf{g}^{(0)\top} M^{-1} \mathbf{g}^{(0)}}{\mathbf{g}^{(0)\top} M^{-1} \mathbf{g}^{(0)}} = -1,$$

which satisfies (19). Assume the induction hypothesis (19) holds for $k = n$. Then, for $k = n+1$, with (16b) and (16c), we have

$$\begin{aligned} \frac{\nabla E_I(\mathbf{f}^{(n+1)})^\top \mathbf{p}^{(n+1)}}{\|\nabla E_I(\mathbf{f}^{(n+1)})\|_{M^{-1}}^2} &= \frac{-\mathbf{g}^{(n+1)\top} M^{-1} \mathbf{g}^{(n+1)}}{\mathbf{g}^{(n+1)\top} M^{-1} \mathbf{g}^{(n+1)}} + \beta_{n+1} \frac{\nabla E_I(\mathbf{f}^{(n+1)})^\top \mathbf{p}^{(n)}}{\|\nabla E_I(\mathbf{f}^{(n+1)})\|_{M^{-1}}^2} \\ &= -1 + \frac{\mathbf{g}^{(n+1)\top} M^{-1} \mathbf{g}^{(n+1)}}{\mathbf{g}^{(n)\top} M^{-1} \mathbf{g}^{(n)}} \frac{\nabla E_I(\mathbf{f}^{(n+1)})^\top \mathbf{p}^{(n)}}{\mathbf{g}^{(n+1)\top} M^{-1} \mathbf{g}^{(n+1)}} = -1 + \frac{\nabla E_I(\mathbf{f}^{(n+1)})^\top \mathbf{p}^{(n)}}{\|\nabla E_I(\mathbf{f}^{(n)})\|_{M^{-1}}^2}. \end{aligned} \quad (20)$$

Then, the second Wolfe condition (18b) implies $|\nabla E_I(\mathbf{f}^{(n+1)})^\top \mathbf{p}^{(n)}| \leq -c_2 \nabla E_I(\mathbf{f}^{(n)})^\top \mathbf{p}^{(n)}$, i.e.,

$$c_2 \nabla E_I(\mathbf{f}^{(n)})^\top \mathbf{p}^{(n)} \leq \nabla E_I(\mathbf{f}^{(n+1)})^\top \mathbf{p}^{(n)} \leq -c_2 \nabla E_I(\mathbf{f}^{(n)})^\top \mathbf{p}^{(n)}. \quad (21)$$

As a result, from (20) and (21), we have

$$-1 + c_2 \frac{\nabla E_I(\mathbf{f}^{(n)})^\top \mathbf{p}^{(n)}}{\|\nabla E_I(\mathbf{f}^{(n)})\|_{M^{-1}}^2} \leq \frac{\nabla E_I(\mathbf{f}^{(n+1)})^\top \mathbf{p}^{(n+1)}}{\|\nabla E_I(\mathbf{f}^{(n+1)})\|_{M^{-1}}^2} \leq -1 - c_2 \frac{\nabla E_I(\mathbf{f}^{(n)})^\top \mathbf{p}^{(n)}}{\|\nabla E_I(\mathbf{f}^{(n)})\|_{M^{-1}}^2}.$$

Then, from the induction hypothesis (19) with $k = n$, we have

$$-\frac{1}{1-c_2} = -1 - \frac{c_2}{1-c_2} \leq \frac{\nabla E_I(\mathbf{f}^{(n+1)})^\top \mathbf{p}^{(n+1)}}{\|\nabla E_I(\mathbf{f}^{(n+1)})\|_{M^{-1}}^2} \leq -1 + \frac{c_2}{1-c_2} = \frac{2c_2-1}{1-c_2},$$

i.e., (19) holds for $k = n+1$. \square

By applying Lemma 3 with a value c_2 chosen in $(0, \frac{1}{2})$, the vector $\mathbf{p}^{(k)}$ could be guaranteed to be a descent direction of E_I at $\mathbf{f}^{(k)}$, which is introduced in the following corollary.

Corollary 1. *Let M be a symmetric positive definite matrix. Suppose the step length α_k satisfies the strong Wolfe conditions (18) with $0 < c_2 < \frac{1}{2}$. Then, $\mathbf{p}^{(k)}$ is a descent direction of E_I at $\mathbf{f}^{(k)}$.*

Proof. We define a monotonically increasing function $\varphi(x) = \frac{2x-1}{1-x}$ on $[0, \frac{1}{2}]$ with $\varphi(0) = -1$ and $\varphi(\frac{1}{2}) = 0$. Then, the second inequality of (19) with $0 < c_2 < \frac{1}{2}$ implies

$$\frac{\nabla E_I(\mathbf{f}^{(k)})^\top \mathbf{p}^{(k)}}{\|\nabla E_I(\mathbf{f}^{(k)})\|_{M^{-1}}^2} \leq \frac{2c_2-1}{1-c_2} = \varphi(c_2) < \varphi(\frac{1}{2}) = 0.$$

Thus, $\nabla E_I(\mathbf{f}^{(k)})^\top \mathbf{p}^{(k)} < 0$, and hence $\mathbf{p}^{(k)}$ is a descent direction of E_I at $\mathbf{f}^{(k)}$. \square

For each iteration of the IEM algorithm, Corollary 1 and Lemma 2 guarantee the existence of step lengths satisfying the strong Wolfe condition (18) with $0 < c_1 < c_2 < \frac{1}{2}$. The Lipschitz continuities of E_I and ∇E_I could be applied to describe further the directional difference between $\mathbf{p}^{(k)}$ and ∇E_I , which is a variant of the Zoutendijk's condition and serves as a core stone for the proof of the global convergence of the preconditioned nonlinear CG method of the IEM.

Lemma 4 (modified Zoutendijk's condition). *Let M be a symmetric positive definite matrix. Suppose the step length α_k satisfies the strong Wolfe conditions (18) with $0 < c_1 < c_2 < \frac{1}{2}$. Then,*

$$\sum_{k=0}^{\infty} \cos^2 \theta_M^{(k)} \|\nabla E_I(\mathbf{f}^{(k)})\|_{M^{-1}}^2 < \infty, \quad (22a)$$

where $\cos \theta_M^{(k)}$ is defined as

$$\cos \theta_M^{(k)} = -\frac{\nabla E_I(\mathbf{f}^{(k)})^\top \mathbf{p}^{(k)}}{\|\nabla E_I(\mathbf{f}^{(k)})\|_{M^{-1}} \|\mathbf{p}^{(k)}\|_M}, \quad (22b)$$

provided that $\mathbf{p}^{(k)}$ is given by (16).

Proof. The step length α_k satisfies the Wolfe condition (18), by Corollary 1, $\mathbf{p}^{(k)}$ is a descent direction and thus the second Wolfe condition (18b) holds, i.e.,

$$\nabla E_I(\mathbf{f}^{(k+1)})^\top \mathbf{p}^{(k)} \geq c_2 \nabla E_I(\mathbf{f}^{(k)})^\top \mathbf{p}^{(k)}. \quad (23)$$

By subtracting $\nabla E_I(\mathbf{f}^{(k)})^\top \mathbf{p}^{(k)}$ to both sides of (23), we obtain

$$(\nabla E_I(\mathbf{f}^{(k+1)}) - \nabla E_I(\mathbf{f}^{(k)}))^\top \mathbf{p}^{(k)} \geq (c_2 - 1) \nabla E_I(\mathbf{f}^{(k)})^\top \mathbf{p}^{(k)}. \quad (24)$$

Since ∇E_I is Lipschitz continuous, (24) implies

$$(c_2 - 1) \nabla E_I(\mathbf{f}^{(k)})^\top \mathbf{p}^{(k)} \leq \|\nabla E_I(\mathbf{f}^{(k+1)}) - \nabla E_I(\mathbf{f}^{(k)})\| \|\mathbf{p}^{(k)}\| \leq C \|\mathbf{f}^{(k+1)} - \mathbf{f}^{(k)}\| \|\mathbf{p}^{(k)}\|. \quad (25)$$

The values in (25) can be estimated in M -norm as

$$\|\mathbf{f}^{(k+1)} - \mathbf{f}^{(k)}\| = \|M^{-1/2}(\mathbf{f}^{(k+1)} - \mathbf{f}^{(k)})\|_M \leq \|M^{-1/2}\|_M \|\mathbf{f}^{(k+1)} - \mathbf{f}^{(k)}\|_M, \quad (26)$$

and

$$\|\mathbf{p}^{(k)}\| = \|M^{-1/2} \mathbf{p}^{(k)}\|_M \leq \|M^{-1/2}\|_M \|\mathbf{p}^{(k)}\|_M. \quad (27)$$

From (23)–(26), we have

$$\alpha_k = \frac{\|\mathbf{f}^{(k+1)} - \mathbf{f}^{(k)}\|_M}{\|\mathbf{p}^{(k)}\|_M} = \frac{\|\mathbf{f}^{(k+1)} - \mathbf{f}^{(k)}\|_M \|\mathbf{p}^{(k)}\|_M}{\|\mathbf{p}^{(k)}\|_M^2} \geq \frac{c_2 - 1}{C \|M^{-1/2}\|_M^2} \frac{\nabla E_I(\mathbf{f}^{(k)})^\top \mathbf{p}^{(k)}}{\|\mathbf{p}^{(k)}\|_M^2}. \quad (28)$$

By substituting (28) into the first Wolfe condition (18a), we obtain

$$\begin{aligned} E_I(\mathbf{f}^{(k+1)}) &\leq E_I(\mathbf{f}^{(k)}) - c_1 \frac{1 - c_2}{C \|M^{-1/2}\|_M^2} \frac{\nabla E_I(\mathbf{f}^{(k)})^\top \mathbf{p}^{(k)}}{\|\mathbf{p}^{(k)}\|_M^2} \nabla E_I(\mathbf{f}^{(k)})^\top \mathbf{p}^{(k)} \\ &\leq E_I(\mathbf{f}^{(k)}) - \tilde{C} \frac{(\nabla E_I(\mathbf{f}^{(k)})^\top \mathbf{p}^{(k)})^2}{\|\mathbf{p}^{(k)}\|_M^2} = E_I(\mathbf{f}^{(k)}) - \tilde{C} \cos^2 \theta_M^{(k)} \|\nabla E_I(\mathbf{f}^{(k)})\|_{M^{-1}}^2, \end{aligned} \quad (29)$$

where $\tilde{C} = \frac{c_1(1-c_2)}{C \|M^{-1/2}\|_M^2} > 0$ and $\cos \theta_M^{(k)}$ is defined as (22b). The recursive inequality (29) implies

$$E_I(\mathbf{f}^{(k+1)}) \leq E_I(\mathbf{f}^{(0)}) - \tilde{C} \sum_{j=0}^k \cos^2 \theta_M^{(j)} \|\nabla E_I(\mathbf{f}^{(j)})\|_{M^{-1}}^2.$$

In other words,

$$\sum_{j=0}^k \cos^2 \theta_M^{(j)} \|\nabla E_I(\mathbf{f}^{(j)})\|_{M^{-1}}^2 = \frac{1}{\tilde{C}} (E_I(\mathbf{f}^{(0)}) - E_I(\mathbf{f}^{(k+1)})). \quad (30)$$

Since $E_I(\mathbf{f}) \geq 0$ is bounded below, the value $E_I(\mathbf{f}^{(0)}) - E_I(\mathbf{f}^{(k+1)})$ in (30) is bounded above. Therefore,

$$\lim_{k \rightarrow \infty} \sum_{j=0}^k \cos^2 \theta_M^{(j)} \leq \sup_{\mathbf{f}} \frac{1}{\tilde{C}} (E_I(\mathbf{f}^{(0)}) - E_I(\mathbf{f})) < \infty,$$

which is equivalent to (22). \square

Lemma 4 would guarantee the global convergence of the iteration if $\mathbf{p}^{(k)}$ is parallel to $\nabla E(\mathbf{f}^{(k)})$ in M^{-1} -norm, i.e. $\mathbf{p}^{(k)} = -M^{-1} \nabla E(\mathbf{f}^{(k)})$, since $\cos \theta_M^{(k)} = 1$. For the non-linear CG method with preconditioners, the correction term makes $\mathbf{p}^{(k)}$ deviate from the vector $-M^{-1} \nabla E(\mathbf{f}^{(k)})$ while $\cos \theta_M^{(k)} > 0$ due to descent direction $\mathbf{p}^{(k)}$. To guarantee that $\|\nabla E(\mathbf{f}^{(k)})\|_{M^{-1}}$ vanishes as k tends to infinite, in the following theorem, we apply the first inequality of (19) in Lemma 3 to show that $\cos \theta_M^{(k)}$ would not vanish and establish the global convergence of the iteration of IEM.

Theorem 2. *Suppose the step length α_k satisfies the strong Wolfe conditions (18) with $0 < c_1 < c_2 < \frac{1}{2}$. Then,*

$$\liminf_{k \rightarrow \infty} \|\nabla E_I(\mathbf{f}^{(k)})\|_{M^{-1}} = 0, \quad (31)$$

provided that M is a symmetric positive definite matrix.

Proof. We prove (31) by contradiction. Assume on the contrary that

$$\liminf_{k \rightarrow \infty} \|\nabla E_A(\mathbf{f}^{(k)})\|_{M-1} \neq 0,$$

i.e., there is a natural number N and a positive real number γ such that

$$\|\nabla E_I(\mathbf{f}^{(k)})\|_{M-1} \geq \gamma, \quad (32)$$

for every $k > N$. Let $\theta_M^{(k)}$ be defined as (22b). Then, by Lemma 3 and (22b), we have

$$-\frac{1}{1-c_2} \leq \frac{\nabla E_I(\mathbf{f}^{(k)})^\top \mathbf{p}^{(k)}}{\|\nabla E_I(\mathbf{f}^{(k)})\|_{M-1}^2} \leq \frac{2c_2-1}{1-c_2},$$

i.e.,

$$-\frac{1}{1-c_2} \leq -\cos \theta_M^{(k)} \frac{\|\mathbf{p}^{(k)}\|_M}{\|\nabla E_I(\mathbf{f}^{(k)})\|_{M-1}} \leq \frac{2c_2-1}{1-c_2},$$

which leads to

$$\frac{1-2c_2}{1-c_2} \frac{\|\nabla E_I(\mathbf{f}^{(k)})\|_{M-1}}{\|\mathbf{p}^{(k)}\|_M} \leq \cos \theta_M^{(k)} \leq \frac{1}{1-c_2} \frac{\|\nabla E_I(\mathbf{f}^{(k)})\|_{M-1}}{\|\mathbf{p}^{(k)}\|_M}. \quad (33)$$

By (22) in Lemma 4 and (33), we obtain

$$\sum_{k=0}^{\infty} \frac{\|\nabla E_I(\mathbf{f}^{(k)})\|_{M-1}^4}{\|\mathbf{p}^{(k)}\|_M^2} < \infty. \quad (34)$$

Then, (32) and (34) lead to

$$\sum_{k=0}^{\infty} \frac{1}{\|\mathbf{p}^{(k)}\|_M^2} < \infty. \quad (35)$$

On the other hand, the second inequality of (19) in Lemma 3 implies

$$-\nabla E_I(\mathbf{f}^{(k)})^\top \mathbf{p}^{(k)} \leq \frac{1}{1-c_2} \|\nabla E_I(\mathbf{f}^{(k)})\|_{M-1}^2. \quad (36)$$

Then, the second Wolfe condition (18b) and (36) imply

$$|\nabla E_I(\mathbf{f}^{(k)})^\top \mathbf{p}^{(k-1)}| \leq -c_2 \nabla E_I(\mathbf{f}^{(k-1)})^\top \mathbf{p}^{(k-1)} \leq \frac{c_2}{1-c_2} \|\nabla E_I(\mathbf{f}^{(k-1)})\|_{M-1}^2. \quad (37)$$

The M -norm of $\mathbf{p}^{(k)} = -M^{-1} \nabla E_I(\mathbf{f}^{(k)}) + \beta_k \mathbf{p}^{(k-1)}$ can be estimated by

$$\begin{aligned} \|\mathbf{p}^{(k)}\|_M^2 &= \|M^{-1} \nabla E_I(\mathbf{f}^{(k)})\|_M^2 - 2\beta_k (M^{-1} \nabla E_I(\mathbf{f}^{(k)}))^\top (M \mathbf{p}^{(k-1)}) + \beta_k^2 \|\mathbf{p}^{(k-1)}\|_M^2 \\ &\leq \|\nabla E_I(\mathbf{f}^{(k)})\|_{M-1}^2 + 2\beta_k |\nabla E_I(\mathbf{f}^{(k)})^\top \mathbf{p}^{(k-1)}| + \beta_k^2 \|\mathbf{p}^{(k-1)}\|_M^2, \end{aligned} \quad (38)$$

where β_k in (16c) is equivalent to

$$\beta_k = \frac{\|\nabla E_I(\mathbf{f}^{(k)})\|_{M-1}^2}{\|\nabla E_I(\mathbf{f}^{(k-1)})\|_{M-1}^2}. \quad (39)$$

Then, (37), (38) and (39) imply

$$\begin{aligned} \|\mathbf{p}^{(k)}\|_M^2 &\leq \|\nabla E_I(\mathbf{f}^{(k)})\|_{M-1}^2 + \frac{2c_2}{1-c_2} \beta_k \|\nabla E_I(\mathbf{f}^{(k-1)})\|_{M-1}^2 + \beta_k^2 \|\mathbf{p}^{(k-1)}\|_M^2 \\ &= \|\nabla E_I(\mathbf{f}^{(k)})\|_{M-1}^2 + \frac{2c_2}{1-c_2} \|\nabla E_I(\mathbf{f}^{(k)})\|_{M-1}^2 + \beta_k^2 \|\mathbf{p}^{(k-1)}\|_M^2 \\ &= \left(\frac{1+c_2}{1-c_2}\right) \|\nabla E_I(\mathbf{f}^{(k)})\|_{M-1}^2 + \beta_k^2 \|\mathbf{p}^{(k-1)}\|_M^2. \end{aligned} \quad (40)$$

Let $c_3 = (1+c_2)/(1-c_2)$. Then c_3 is positive. The recursive inequality (40) with the initial vector $\mathbf{p}^{(0)} = M^{-1} \nabla E_I(\mathbf{f}^{(0)})$ implies

$$\|\mathbf{p}^{(k)}\|_M^2 \leq c_3 \sum_{i=0}^k \left(\prod_{j=i+1}^k \beta_j^2 \right) \|\nabla E_I(\mathbf{f}^{(i)})\|_{M-1}^2. \quad (41)$$

It can be derived from the expression of β_k in (39) that

$$\prod_{j=i+1}^k \beta_j^2 = \frac{\|\nabla E_I(\mathbf{f}^{(k)})\|_{M-1}^4}{\|\nabla E_I(\mathbf{f}^{(i)})\|_{M-1}^4}. \quad (42)$$

By substituting the product of β_k in (41) with (42), we obtain

$$\|\mathbf{p}^{(k)}\|_M^2 \leq c_3 \|\nabla E_I(\mathbf{f}^{(k)})\|_{M-1}^4 \sum_{i=0}^k \frac{1}{\|\nabla E_I(\mathbf{f}^{(i)})\|_{M-1}^2}. \quad (43)$$

In addition, since $\|\nabla E_I(\mathbf{f}^{(k)})\|_{M-1}^2 \leq \|\nabla E_I(\mathbf{f}^{(j)})\|_{M-1}^2$ for $j \leq k$ and $k > N$, then, the assumption (32) implies

$$\sum_{i=0}^k \frac{1}{\|\nabla E_I(\mathbf{f}^{(i)})\|_{M-1}^2} \leq \sum_{i=0}^k \frac{1}{\|\nabla E_I(\mathbf{f}^{(k)})\|_{M-1}^2} \leq \frac{k}{\gamma^2}, \quad \text{for } k > N. \quad (44)$$

Note that Lemma 1 tells that ∇E_I is Lipschitz continuous, and the domain of ∇E_I is bounded, there exists $\bar{\gamma}$ such that $\|\nabla E_I(\mathbf{f}^{(k)})\|_{M-1} \leq \bar{\gamma}$ for all k . Consequently, from (43) and (44), for $k > N$,

$$\|\mathbf{p}^{(k)}\|_M^2 \leq \frac{c_3 \bar{\gamma}^4}{\gamma^2} k,$$

which implies

$$\sum_{k=1}^{\infty} \frac{1}{\|\mathbf{p}^{(k)}\|_M^2} \geq \omega \sum_{k=1}^{\infty} \frac{1}{k},$$

for some $\omega > 0$, which contradicts to (35). \square

The global convergence of the proposed IEM (Algorithm 1) is directly guaranteed by Theorem 2, which is summarized in the following corollary.

Corollary 2. *Assume each step length satisfying the strong Wolfe conditions (18) with $0 < c_1 < c_2 < \frac{1}{2}$, the preconditioned nonlinear CG method, Algorithm 1 converges globally.*

6 Numerical Experiments

In this section, we present the numerical results of the proposed preconditioned nonlinear CG method for IEM, Algorithm 1. The benchmark tetrahedral mesh models demonstrated in Figure 3 are from Jacobson's GitHub [18], Gu's website [15], and the BraTS databases [2, 3]. Some tetrahedral mesh models are generated by using the `iso2mesh` [12, 25] and `JIGSAW` mesh generators [8, 7, 9, 10, 11]. All the experiments are performed in MATLAB on a laptop with AMD Ryzen 9 5900HS and 32 GB RAM.

To quantify the local volume distortion of a mapping f , we compute the relative difference between the volumes of τ and $f(\tau)$ as

$$D_V(f, \tau) = \left| \frac{|f(\tau)|/\mathcal{V}(f) - |\tau|/\mathcal{V}(e)}{|\tau|/\mathcal{V}(e)} \right|. \quad (45)$$

A volume-preserving mapping f has the property that $D_V(f, \tau) = 0$, for every $\tau \in \mathbb{T}(\mathcal{M})$.

Figure 4 demonstrates the histograms of the local volume distortions (45) of the mappings computed by the proposed IEM, Algorithm 1 with 500 iterations. It shows that most of the relative volume differences produced by the mappings are less than 0.1. Table 1 further shows the 25th, 50th, 75th, and 95th percentiles of $D_V(f, \tau)$ (45), respectively. In particular, the 95th percentile indicates that at least 95% tetrahedra have local distortions of the magnitude 10^{-2} in volume ratios, which is quite satisfactory.

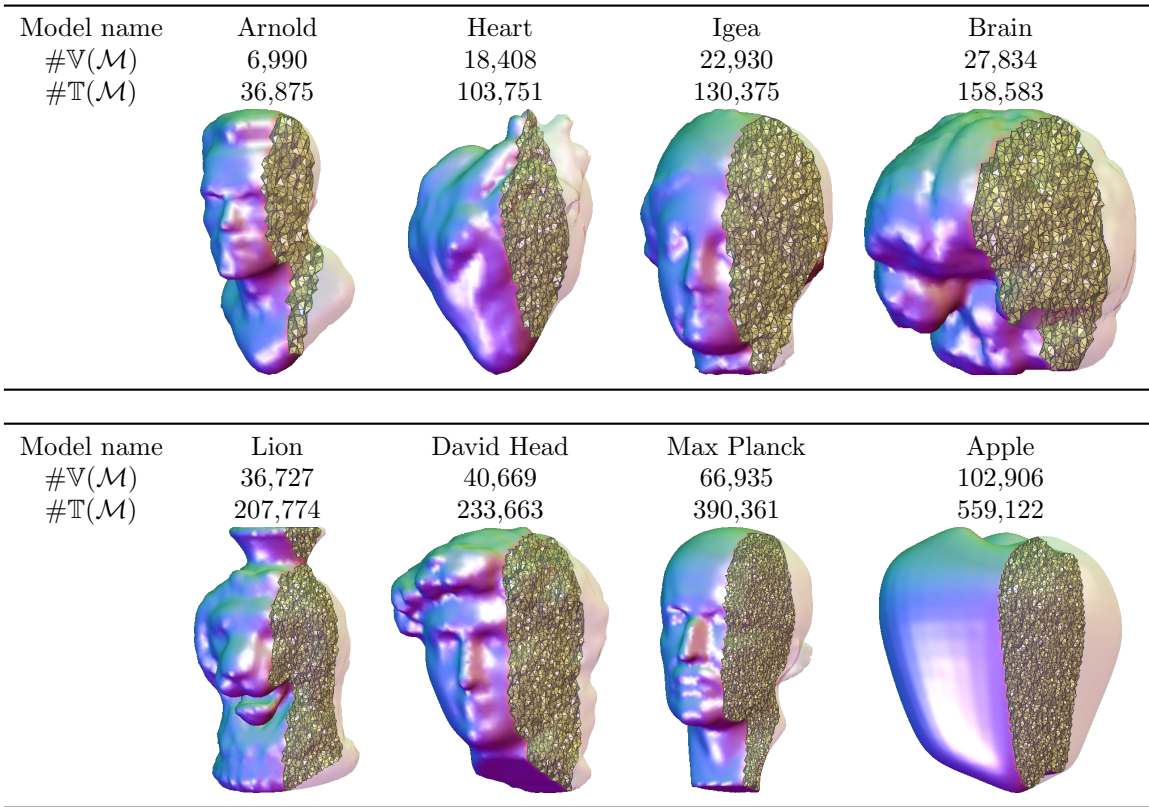


Figure 3: The benchmark tetrahedral mesh models.

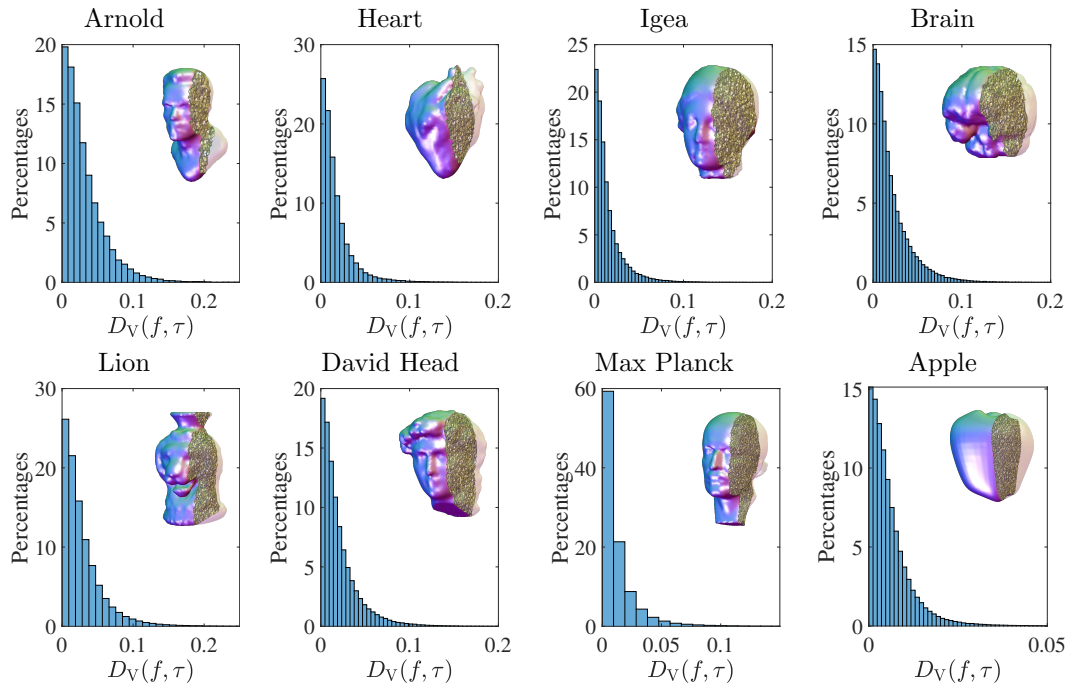


Figure 4: Histograms of the local volume distortion $D_V(f, \tau)$ (45) of the mappings computed by the IEM, Algorithm 1.

Table 1: The 25th, 50th, 75th, and 95th percentiles of the local volume distortion $D_V(f, \tau)$ (45) of the mappings produced by the IEM, Algorithm 1.

Model name	Percentiles of the local volume distortion $D_V(f, \tau)$			
	25th	50th	75th	95th
Arnold	1.07×10^{-2}	2.33×10^{-2}	4.33×10^{-2}	8.86×10^{-2}
Heart	5.15×10^{-3}	1.14×10^{-2}	2.17×10^{-2}	5.23×10^{-2}
Igea	4.26×10^{-3}	9.63×10^{-3}	1.93×10^{-2}	4.87×10^{-2}
Brain	6.32×10^{-3}	1.43×10^{-2}	2.85×10^{-2}	6.35×10^{-2}
Lion	9.01×10^{-3}	2.01×10^{-2}	3.84×10^{-2}	8.52×10^{-2}
David Head	6.21×10^{-3}	1.40×10^{-2}	2.74×10^{-2}	6.32×10^{-2}
Max Planck	3.14×10^{-3}	7.29×10^{-3}	1.55×10^{-2}	4.26×10^{-2}
Apple	1.98×10^{-3}	4.33×10^{-3}	8.00×10^{-3}	1.73×10^{-2}

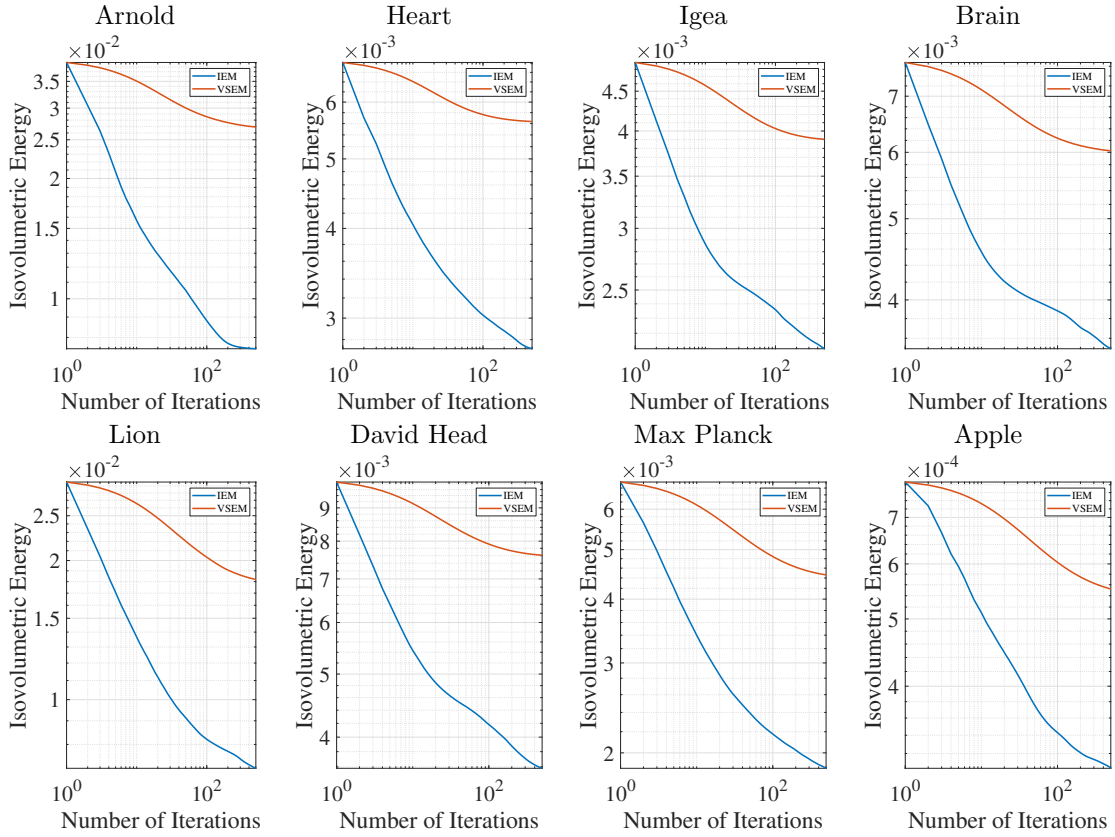


Figure 5: Relationship between the isovolumetric energy and the number of iterations of the IEM and VSEM algorithms, respectively.

Table 2: The mean and SD of local volume distortion (45) and isovolumetric energy (2) of mappings produced by our proposed IEM (Algorithm 1) and the fixed-point method [28, Algorithm 4.4], with 500 iterations.

Model name	Proposed IEM (Algorithm 1)				Fixed-point method of VSEM [28, Algorithm 4.4]			
	Volume distortion $D_V(f, \tau)$		$E_I(f)$	#Fold-ings	Volume distortion $D_V(f, \tau)$		$E_I(f)$	#Fold-ings
	Mean	SD			Mean	SD		
Arnold	3.17×10^{-2}	3.07×10^{-2}	7.50×10^{-3}	0	5.82×10^{-2}	6.60×10^{-2}	2.69×10^{-2}	2
Heart	1.73×10^{-2}	2.07×10^{-2}	2.78×10^{-3}	0	2.30×10^{-2}	3.40×10^{-2}	5.87×10^{-3}	1
Igea	1.52×10^{-2}	1.77×10^{-2}	2.10×10^{-3}	0	1.86×10^{-2}	2.65×10^{-2}	3.90×10^{-3}	0
Brain	2.11×10^{-2}	2.18×10^{-2}	3.50×10^{-3}	0	2.66×10^{-2}	3.11×10^{-2}	6.02×10^{-3}	0
Lion	2.89×10^{-2}	3.13×10^{-2}	7.10×10^{-2}	0	4.27×10^{-2}	5.39×10^{-2}	1.82×10^{-2}	5
David Head	2.05×10^{-2}	2.22×10^{-2}	3.52×10^{-3}	0	2.55×10^{-2}	3.38×10^{-2}	6.81×10^{-3}	0
Max Planck	1.28×10^{-2}	1.78×10^{-2}	1.87×10^{-3}	0	1.78×10^{-2}	3.02×10^{-2}	4.46×10^{-3}	6
Apple	6.00×10^{-3}	6.20×10^{-3}	3.06×10^{-4}	0	7.60×10^{-3}	9.00×10^{-3}	5.48×10^{-4}	0

6.1 Comparison to the state-of-the-art

To the best of our knowledge, the fixed-point method of the VSEM [28, Algorithm 4.4] is the state-of-the-art method with the best effectiveness and accuracy for computing ball-shaped volume-preserving parameterizations of simplicial 3-manifolds. Comparison of the VSEM [28, Algorithm 4.4] to another state-of-the-art method, the OMT-based method [24, Algorithm 4], can be found in [28, Section 6], which indicates that the VSEM is significantly more effective and accurate than the OMT-based method [24, Algorithm 4] on computing ball-shaped volume-preserving parameterizations.

In this subsection, we compare the proposed IEM, Algorithm 1, to the fixed-point method of the VSEM [28, Algorithm 4.4]. The number of iterations for both algorithms is set to 500. The initial mapping is computed by the fixed-point method of VSEM [28] with 15 iterations.

The relationship between the isovolumetric energy and the number of iterations is demonstrated in Figure 5, which indicates that the proposed IEM is significantly more effective in decreasing the energy (2).

In addition, the mean and standard deviation (SD) of local volume distortion (45), the isovolumetric energy E_I (2), and the number of folding tetrahedra of resulting mappings are further demonstrated in Table 2 and visualized in Figures 6 and 7. We observe that our proposed IEM has significant improvement in terms of accuracy and bijectivity. On average, our proposed IEM improves 53%, 26%, and 38%, in terms of energy, mean, and SD of local volume distortion, respectively, relative to that of the fixed-point method of the VSEM [28, Algorithm 4.4].

Furthermore, we compare the computational time costs of the proposed IEM and the VSEM [28] in Figure 6. The results are consistent with the computational complexity of $O(n^3)$ for both algorithms. This indicates that the efficiency of the proposed IEM is competitive with that of the VSEM [28].

On the other hand, to present the utility of the AST (11) on improving the bijectivity, in Table 3, we further demonstrate the numerical results in the above metrics without performing the AST (11) in Steps 1–3 of Algorithm 1. Comparing the results in Table 3 to those with the AST in Table 2, we observe that the volume-preserving qualities are similar in both tables. However, the bijectivity of mappings produced by the proposed IEM is significantly improved and achieves completely bijective mappings. These results demonstrate the great utility of the AST (11) in enhancing the bijectivity in the proposed IEM.

The comparison between the number of folding tetrahedra with and without performing the AST for five particular models is further visualized in Figure 8, which indicates that the AST (11) shows little utility in improving the bijectivity of mappings produced by the fixed-point method [28] of VSEM. These results indicate that both the boundary updating and the AST (11) are crucial in achieving bijective volume-preserving ball-shaped mappings. To the best of our knowledge, there is no algorithm for tetrahedral mappings that could theoretically guarantee the bijectivity of the produced mapping. Still, numerical results of the proposed IEM indicate that the volume-preserving property might potentially provide a way to achieve orientation-preserving tetrahedral mappings.

Table 3: The mean and SD of local volume distortion (45) and isovolumetric energy (2) of mappings produced by our proposed IEM (Algorithm 1) and the fixed-point method [28, Algorithm 4.4], with 500 iterations, without performing the AST (11).

Model name	Proposed IEM (Algorithm 1)				Fixed-point method of VSEM [28, Algorithm 4.4]			
	Volume distortion Mean	$D_V(f, \tau)$ SD	$E_I(f)$	#Fold- ings	Volume distortion Mean	$D_V(f, \tau)$ SD	$E_I(f)$	#Fold- ings
Arnold	3.16×10^{-2}	3.07×10^{-2}	7.49×10^{-3}	0	5.14×10^{-2}	6.10×10^{-2}	2.13×10^{-2}	2
Heart	1.72×10^{-2}	2.04×10^{-2}	2.72×10^{-3}	0	2.10×10^{-2}	3.31×10^{-2}	5.16×10^{-3}	1
Igea	1.52×10^{-2}	1.80×10^{-2}	2.15×10^{-3}	0	1.86×10^{-2}	2.64×10^{-2}	3.86×10^{-3}	0
Brain	2.07×10^{-2}	2.15×10^{-2}	3.40×10^{-3}	0	2.56×10^{-2}	3.93×10^{-2}	5.43×10^{-3}	0
Lion	2.85×10^{-2}	3.05×10^{-2}	6.79×10^{-2}	2	3.89×10^{-2}	4.97×10^{-2}	1.53×10^{-2}	5
David Head	2.05×10^{-2}	2.21×10^{-2}	3.51×10^{-3}	0	2.51×10^{-2}	3.31×10^{-2}	6.55×10^{-3}	0
Max Planck	1.30×10^{-2}	1.72×10^{-2}	1.82×10^{-3}	0	1.58×10^{-2}	2.83×10^{-2}	3.75×10^{-3}	5
Apple	6.00×10^{-3}	6.00×10^{-3}	2.98×10^{-4}	0	7.60×10^{-3}	9.80×10^{-3}	6.06×10^{-4}	0

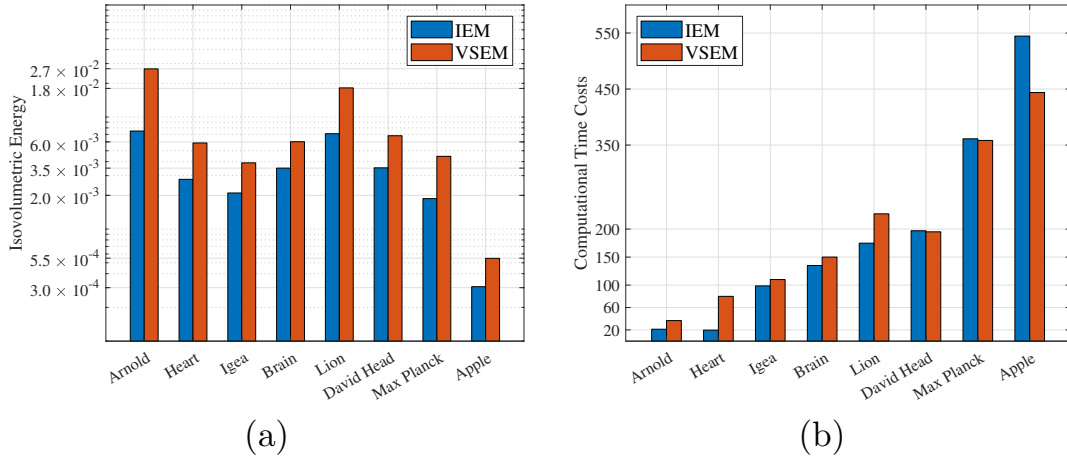


Figure 6: The isovolumetric energy (a) in (2) and computational time costs (b), carried out by the proposed IEM (Algorithm 1) and the fixed-point method of VSEM [30, Algorithm 4.4] among all benchmark models.

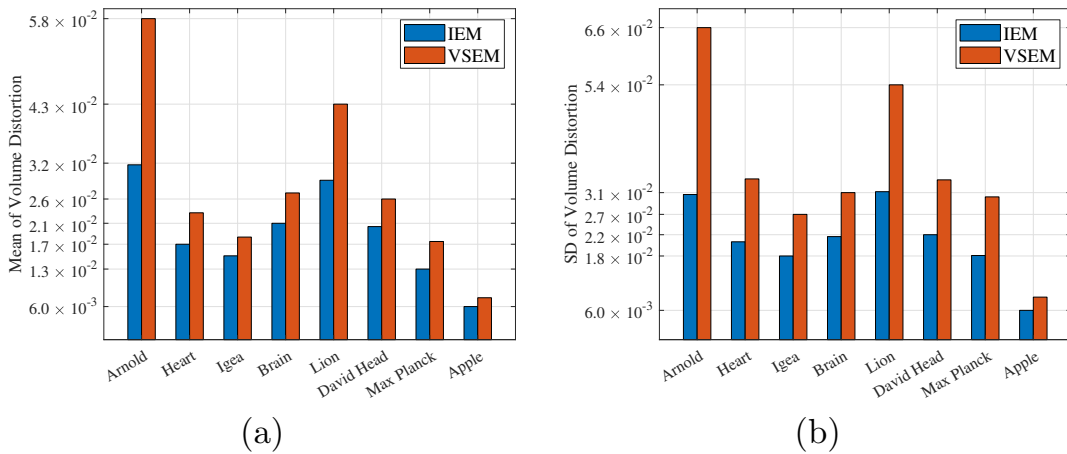


Figure 7: The mean (a) and SD (b) of volume distortion in (45), carried out by the proposed IEM, Algorithm 1, and VSEM [30] among all benchmark models.

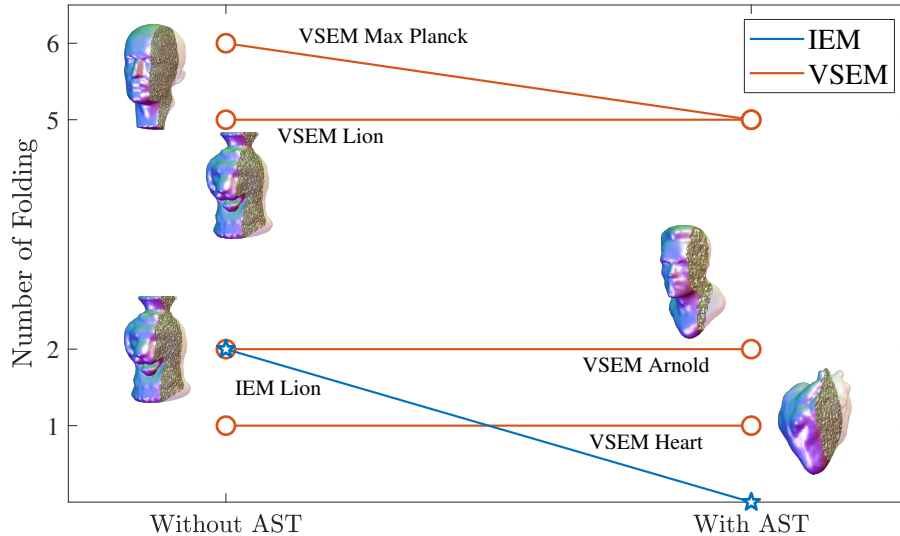


Figure 8: An illustration of comparison in terms of numbers of folding tetrahedra of mappings produced by the proposed IEM (Algorithm 1) and the fixed-point method of VSEM [28, Algorithm 4.4] with and without performing the AST (11).

7 Applications to shape registration and deformation

The ball-shaped parameterization computed by the IEM is unique up to a rotation transformation. Based on this fact, each rotation transformation in the parameter space defines a volume-preserving registration mapping between manifolds. A natural one-to-one correspondence between two manifolds can then be obtained through an optimal rotation transformation in the parameter space. This mapping also provides a measurement of shape dissimilarity between the manifolds.

In practice, to find the volume-preserving registration mapping between two tetrahedral meshes \mathcal{M}_0 and \mathcal{M}_1 , we first compute the volume-preserving parameterizations $f_s : \mathcal{M}_s \rightarrow \mathbb{B}^3$, $s = 0, 1$, using Algorithm 1. The remaining degrees of freedom on the solid unit ball are rotation transformations in $SO(3)$. To remove such a freedom, we compute the optimal rotations by

$$g_s = \operatorname{argmin}_{g \in SO(3)} \sum_{v \in \mathbb{V}(\mathcal{M}_s)} \|g \circ f_s(v) - v\|_2^2 \operatorname{vol}(v), \quad s = 0, 1,$$

where $\operatorname{vol}(v)$ denotes the vertex volume of v defined by $\operatorname{vol}(v) = \frac{1}{4} \sum_{\tau \ni v} |\tau|$. Then, the rigid registration mapping on \mathbb{B}^3 is given by $h = g_1^{-1} \circ g_0$. Ultimately, the volume-preserving registration mapping $\varphi : \mathcal{M}_0 \rightarrow \mathcal{M}_1$ is given by $\varphi = f_1^{-1} \circ h \circ f_0$, as illustrated in Figure 9.

To visualize the deformation of the mapping φ , one can employ the linear homotopy, defined as

$$\mathcal{H}(v, t) = (1 - t)v + t\varphi(v). \quad (46)$$

In Figure 10, we demonstrate the simplicial 3-manifolds $\mathcal{H}(\mathcal{M}_0, t)$, for $t = 0, \frac{1}{3}, \frac{2}{3}$, and 1, which shows that the deformation is very subtle because the shapes of two given simplicial 3-manifolds are similar. To quantify the deformation resulting from φ , we compute the value

$$d(\varphi) = \frac{\sum_{v \in \mathbb{V}(\mathcal{M}_0)} \|v - \varphi(v)\|_2 \operatorname{vol}(v)}{|\mathcal{M}_0|} = 7.82\%,$$

which is reasonably small.

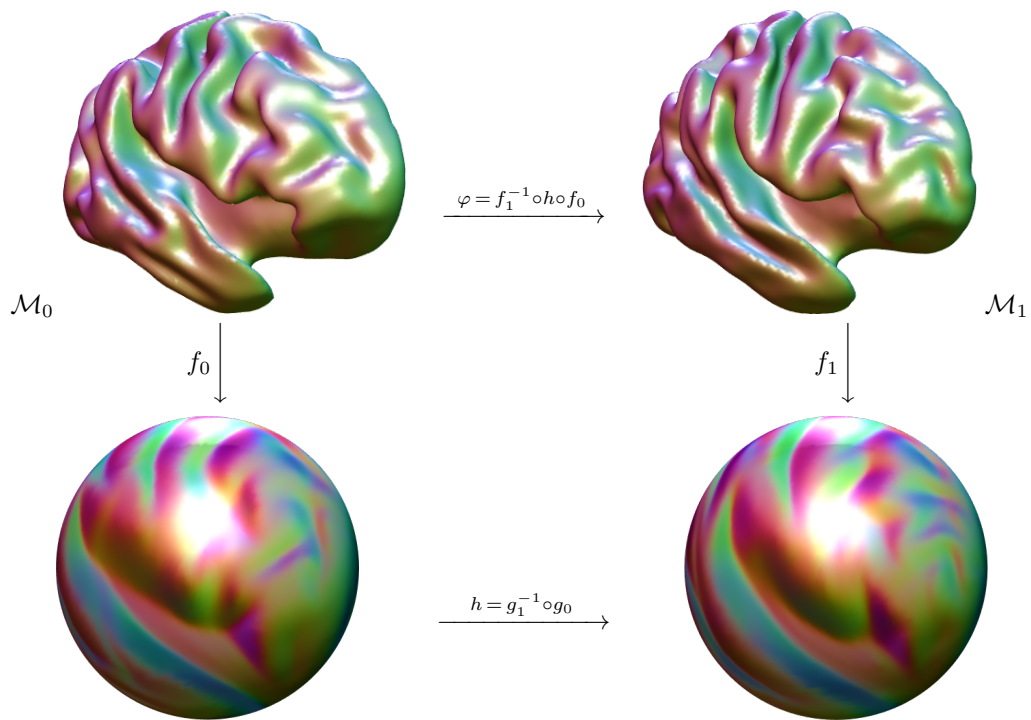


Figure 9: An illustration of the computational procedures of a volume-preserving registration mapping between two simplicial 3-manifolds.

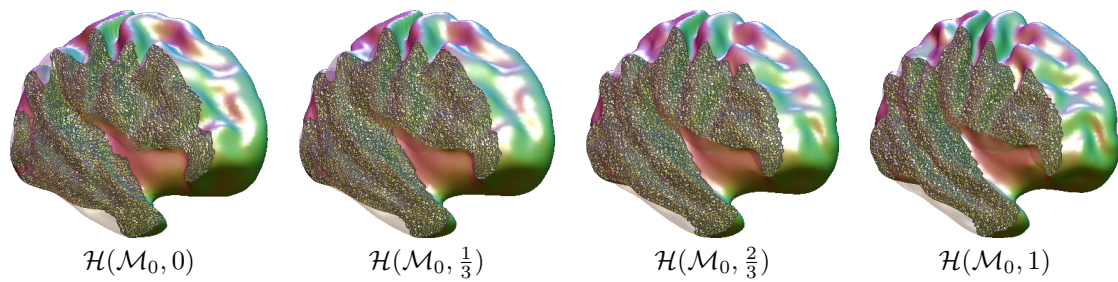


Figure 10: The image of linear homotopy $\mathcal{H}(\mathcal{M}_0, t)$ between the identity mapping and the volume-preserving registration mapping, as defined in (46).

8 Concluding remarks

In this paper, we have formulated the computation of ball-shaped volume-preserving parameterizations as a nonlinear functional minimization problem and developed an efficient preconditioned nonlinear CG method for solving the problem. Convergence analysis is provided to guarantee the global convergence of the proposed algorithm. Numerical experiments demonstrate that our method achieves superior accuracy and computational efficiency compared to a previous representative state-of-the-art algorithm. Additionally, our algorithm shows considerable potential for measuring shape dissimilarity, an essential issue in shape analysis. This highlights the practical utility and effectiveness of our developed IEM algorithm.

Acknowledgement

The work of the authors was supported by the National Science and Technology Council and the National Center for Theoretical Sciences in Taiwan.

References

- [1] S. M. Abulnaga, O. Stein, P. Golland, and J. Solomon. Symmetric volume maps: Order-invariant volumetric mesh correspondence with free boundary. *ACM Trans. Graph.*, 42(3), 2023.
- [2] U. Baid, S. Ghodasara, M. Bilello, S. Mohan, E. Calabrese, E. Colak, K. Farahani, J. Kalpathy-Cramer, F. C. Kitamura, S. Pati, L. M. Prevedello, J. D. Rudie, C. Sako, R. T. Shinohara, T. Bergquist, R. Chai, J. Eddy, J. Elliott, W. Reade, T. Schaffter, T. Yu, J. Zheng, B. Annotators, C. Davatzikos, J. Mongan, C. Hess, S. Cha, J. Villanueva-Meyer, J. B. Freymann, J. S. Kirby, B. Wiestler, P. Crivellaro, R. R. Colen, A. Kotrotsou, D. Marcus, M. Milchenko, A. Nazeri, H. Fathallah-Shaykh, R. Wiest, A. Jakob, M.-A. Weber, A. Mahajan, B. Menze, A. E. Flanders, and S. Bakas. The RSNA-ASNR-MICCAI BraTS 2021 benchmark on brain tumor segmentation and radiogenomic classification, 2021.
- [3] S. Bakas, H. Akbari, A. Sotiras, M. Bilello, M. Rozycki, J. S. Kirby, J. B. Freymann, K. Farahani, and C. Davatzikos. Advancing the cancer genome Atlas glioma MRI collections with expert segmentation labels and radiomic features. *Sci. Data*, 4(170117), 2017.
- [4] M. Campen, C. T. Silva, and D. Zorin. Bijective maps from simplicial foliations. *ACM Trans. Graph.*, 35(4), 2016.
- [5] A. Chern, U. Pinkall, and P. Schröder. Close-to-conformal deformations of volumes. *ACM Trans. Graph.*, 34(4), 2015.
- [6] X. Du, N. Aigerman, Q. Zhou, S. Z. Kovalsky, Y. Yan, D. M. Kaufman, and T. Ju. Lifting simplices to find injectivity. *ACM Trans. Graph.*, 39(4), 2020.
- [7] D. Engwirda. Locally optimal delaunay-refinement and optimisation-based mesh generation. 2014.
- [8] D. Engwirda. Voronoi-based point-placement for three-dimensional delaunay-refinement. *Procedia Engineering*, 124:330–342, 2015.
- [9] D. Engwirda. Conforming restricted delaunay mesh generation for piecewise smooth complexes. *Procedia engineering*, 163:84–96, 2016.
- [10] D. Engwirda and D. Ivers. Face-centred voronoi refinement for surface mesh generation. *Procedia Engineering*, 82:8–20, 2014.
- [11] D. Engwirda and D. Ivers. Off-centre steiner points for delaunay-refinement on curved surfaces. *Computer-Aided Design*, 72:157–171, 2016.
- [12] Q. Fang and D. A. Boas. Tetrahedral mesh generation from volumetric binary and grayscale images. In *2009 IEEE International Symposium on Biomedical Imaging: From Nano to Macro*, pages 1142–1145, 2009.

- [13] X.-M. Fu and Y. Liu. Computing inversion-free mappings by simplex assembly. *ACM Trans. Graph.*, 35(6), 2016.
- [14] V. Garanzha, I. Kaporin, L. Kudryavtseva, F. Protais, N. Ray, and D. Sokolov. Foldover-free maps in 50 lines of code. *ACM Trans. Graph.*, 40(4), 2021.
- [15] X. Gu. *Optimal Mass Transportation Map*. <https://www3.cs.stonybrook.edu/~gu/software/omt/index.html>, 2022.
- [16] X. Gu, F. Luo, J. Sun, and S.-T. Yau. Variational principles for Minkowski type problems, discrete optimal transport, and discrete Monge-Ampère equations. *Asian J. Math.*, 20(2):383–398, 2016.
- [17] T.-M. Huang, W.-H. Liao, W.-W. Lin, M.-H. Yueh, and S.-T. Yau. Convergence analysis of volumetric stretch energy minimization and its associated optimal mass transport. *SIAM J. Imaging Sci.*, 16(3):1825–1855, 2023.
- [18] A. Jacobson. *GitHub Repository for Common 3D Test Models*. <https://github.com/alectjacobson/common-3d-test-models>, 2021.
- [19] W.-W. Lin, C. Juang, M.-H. Yueh, T.-M. Huang, T. Li, S. Wang, and S.-T. Yau. 3D brain tumor segmentation using a two-stage optimal mass transport algorithm. *Sci. Rep.*, 11:14686, 2021.
- [20] W.-W. Lin, J.-W. Lin, T.-M. Huang, T. Li, M.-H. Yueh, and S.-T. Yau. A novel 2-phase residual U-net algorithm combined with optimal mass transportation for 3D brain tumor detection and segmentation. *Sci. Rep.*, 12:6452, 2022.
- [21] S.-Y. Liu and M.-H. Yueh. Convergent authalic energy minimization for disk area-preserving parameterizations. *J. Sci. Comput.*, 100(2), 2024.
- [22] J. Nocedal and S. J. Wright. *Numerical Optimization*. Springer, New York, NY, New York, NY, USA, 2e edition, 2006.
- [23] M. Rabinovich, R. Poranne, D. Panozzo, and O. Sorkine-Hornung. Scalable locally injective mappings. *ACM Trans. Graph.*, 36(2), 2017.
- [24] K. Su, W. Chen, N. Lei, J. Zhang, K. Qian, and X. Gu. Volume preserving mesh parameterization based on optimal mass transportation. *Comput. Aided Design*, 82:42–56, 2017.
- [25] A. P. Tran, S. Yan, and Q. Fang. Improving model-based fnirs analysis using mesh-based anatomical and light-transport models. *Neurophotonics*, 7(1):015008, 2020.
- [26] M.-H. Yueh. Theoretical foundation of the stretch energy minimization for area-preserving simplicial mappings. *SIAM J. Imaging Sci.*, 16(3):1142–1176, 2023.
- [27] M.-H. Yueh, T.-M. Huang, T. Li, W.-W. Lin, and S.-T. Yau. Projected gradient method combined with homotopy techniques for volume-measure-preserving optimal mass transportation problems. *J. Sci. Comput.*, 88(3), 2021.
- [28] M.-H. Yueh, T. Li, W.-W. Lin, and S.-T. Yau. A novel algorithm for volume-preserving parameterizations of 3-manifolds. *SIAM J. Imag. Sci.*, 12(2):1071–1098, 2019.
- [29] M.-H. Yueh, T. Li, W.-W. Lin, and S.-T. Yau. A new efficient algorithm for volume-preserving parameterizations of genus-one 3-manifolds. *SIAM J. Imag. Sci.*, 13(3):1536–1564, 2020.
- [30] M.-H. Yueh, W.-W. Lin, C.-T. Wu, and S.-T. Yau. A novel stretch energy minimization algorithm for equiareal parameterizations. *J. Sci. Comput.*, 78(3):1353–1386, 2019.